Steady-state kinetic characterization and mechanistic modeling of human lactate dehydrogenase A as a reference framework for inhibitor screening

Bioorganic Chemistry 182 (2026) 110489

Contents lists available at ScienceDirect

Bioorganic Chemistry

journal homepage: www.elsevier.com/locate/bioorg

Steady-state kinetic characterization and mechanistic modeling of human lactate dehydrogenase A as a reference framework for inhibitor screening

Chiara Vincenzi [a], Edoardo Bocina [a], Debora Fino [a], Carminna Ottone [b,*], Marco Piumetti [a,*]

[a] Department of Applied Science and Technology, Politecnico di Torino, Corso Duca degli Abruzzi, 24, 10129 Turin, Italy
[b] Escuela de Ingeniería Bioquímica, Pontificia Universidad Católica de Valparaíso, Av. Brasil, 2085, Valparaíso, Chile

ARTICLE INFO

Keywords:
Human lactate dehydrogenase (*h*LDH-A)
Steady-state kinetic evaluation
Enzyme inhibition profiles
Mathematical modeling
Thermal inactivation
Cancer metabolism

ABSTRACT

Human lactate dehydrogenase A (*h*LDH-A) is a key enzyme in cancer-associated metabolic reprogramming, catalyzing the reversible interconversion of pyruvate and lactate coupled with the NADH/NAD^+ redox pair. A rigorous kinetic reference is therefore essential for the reliable evaluation of *h*LDH-A modulation, particularly in the context of enzyme-based drug screening. In this study, the steady-state kinetics of *h*LDH-A were systematically characterized under physiological-like conditions by analyzing both forward and reverse reactions.

Apparent kinetic parameters were determined using the Michaelis–Menten model and Hanes–Woolf linearization, complemented by nonlinear fitting of untransformed data, while intrinsic kinetic constants were extracted assuming an ordered sequential bi–bi mechanism. The results revealed a pronounced preference for the pyruvate-to-lactate reaction, driven primarily by cofactor-dependent steps rather than substrate affinity. The established kinetic framework was subsequently applied to the comparative evaluation of reference LDH inhibitors, enabling discrimination among competitive, non-competitive, and mixed inhibition mechanisms and the determination of inhibition constants. In particular, oxamate exhibited competitive inhibition relative to pyruvate, whereas galloflavin, gossypol, and FX11 exhibited predominantly non-competitive behavior. NHI-2 showed a mixed inhibition pattern. Inhibition constants, determined under pyruvate-variation conditions, ranged from 6.9 to 52.5 μM, with gossypol showing the highest inhibitory potency among the investigated compounds. Based on the determined kinetic parameters, a mechanistic model describing the net reaction rate was developed to simulate the temporal evolution of the enzymatic system. The model captured the main trend of NADH consumption observed experimentally and qualitatively reproduced the distinct kinetic effects associated with competitive and non-competitive inhibition mechanisms.

1. Introduction

Enzymes are essential regulators of all biological processes, controlling both the rates and the directionality of metabolic reactions that sustain cellular functions [1,2]. Due to their central role, alterations in their activity, regulation, or expression are implicated in a wide range of pathological conditions, including metabolic disorders, cancer, neurodegenerative, and inflammatory diseases [3,4]. Consequently, enzymes represent a major class of therapeutic targets, and their modulation through small molecules remains a cornerstone of modern drug discovery [3,5,6].

A detailed understanding of enzyme kinetics is essential for the rational design and evaluation of enzyme-targeted therapeutics. Kinetic parameters provide quantitative insight into catalytic efficiency, substrate affinity, and reaction reversibility, enabling a mechanistic interpretation of enzymatic behavior beyond qualitative activity measurements [7–9]. In the absence of a robust kinetic framework, variations in substrate concentration, cofactor availability, or environmental conditions may lead to ambiguous or misleading interpretations of enzyme activity. This issue becomes particularly relevant for enzymes catalyzing reversible reactions, whose apparent activity reflects a dynamic balance between forward and reverse processes and is therefore highly sensitive to the surrounding chemical environment [10,11]. Establishing a rigorous kinetic description of such systems is a prerequisite for any subsequent evaluation of perturbations to enzyme function, including those induced by external modulators.

Abbreviations: *h*LDH-A, Human lactate dehydrogenase type A.

* Corresponding authors.
E-mail addresses: carminna.ottone@pucv.cl (C. Ottone), marco.piumetti@polito.it (M. Piumetti).

https://doi.org/10.1016/j.bioorg.2026.110489
Received 25 April 2026; Received in revised form 1 September 2026; Accepted 6 September 2026
Available online 7 September 2026

The importance of enzymatic kinetics becomes particularly evident in pathological conditions characterized by metabolic dysregulation. Cancer represents a paradigmatic example, as tumor cells undergo extensive metabolic reprogramming to sustain rapid proliferation while adapting to nutrient-limited environments [12–17]. These metabolic adaptations are largely driven by altered enzymatic activity and regulation, rather than by the emergence of entirely new metabolic pathways, underscoring the central role of enzyme function in cancer biology [18].

The clinical relevance of cancer-associated metabolic alterations is further highlighted by global epidemiological projections, which forecast a substantial worldwide rise in cancer incidence and mortality by 2050, approximately 65–80% and 75–90%, respectively [19]. These considerations motivate the development of robust biochemical tools for the controlled characterization of enzymes involved in cancer-associated metabolism. Among the enzymes involved in cancer-associated metabolic pathways, lactate dehydrogenase (LDH) occupies a central role [17,18,20–23]. LDH catalyzes the reversible conversion of pyruvate into lactate, coupled to the NADH/NAD^+ redox pair, thereby directly linking glycolytic flux to cellular redox homeostasis. This reaction represents a key metabolic node, as it regulates the balance between oxidative metabolism and anaerobic glycolysis while sustaining continuous NAD^+ regeneration required for high glycolytic rates [18,24–26].

The relevance of LDH, in particular its isoform A (LDH-A), becomes particularly evident in the context of the Warburg effect, a hallmark of cancer metabolism characterized by the preferential conversion of pyruvate to lactate even under aerobic conditions [27–29]. LDH-A is predominantly expressed in highly glycolytic tissues and is frequently upregulated in cancer cells. Increased LDH-A expression has been reported in a wide range of solid tumors and is associated with enhanced glycolytic flux, tumor aggressiveness, and poor prognosis [12,14,26,30,31].

By promoting lactate production, LDH-A contributes not only to metabolic rewiring but also to the acidification of the tumor microenvironment. This process facilitates tumor invasion, immune evasion, and resistance to therapy. Given its pivotal role at the intersection of glycolysis, redox balance, and tumor microenvironment remodeling, LDH-A has therefore become a widely investigated biochemical target in studies of cancer-associated metabolism.

Importantly, selective inhibition of LDH-A is considered potentially safe, as individuals with congenital LDH-A deficiency exhibit relatively mild clinical symptoms [31–36]. However, despite the extensive interest in LDH-A as a therapeutic target, a comprehensive and standardized kinetic framework for the evaluation of *h*LDH-A catalysis and inhibition remains limited. Previous studies have often focused on selected aspects of LDH-A behavior, such as one reaction direction, specific substrate or cofactor conditions, or individual inhibitors, rather than integrating forward and reverse kinetics, substrate and cofactor dependence, intrinsic kinetic parameters, inhibition mechanisms, and reaction modeling within a single experimental framework. In addition, assay configurations may differ in pH, temperature, buffer composition, enzyme source, substrate and cofactor concentrations, variable ligand, and the kinetic parameter used to express inhibitor potency. This variability can complicate the interpretation of inhibition mechanisms and limit direct comparison of inhibitor performance across studies. Therefore, a comprehensive and controlled kinetic reference framework is needed to support a more consistent evaluation of *h*LDH-A modulation.

In this study, a detailed kinetic analysis of human LDH-A (*h*LDH-A) is presented, systematically investigating both the forward and reverse catalytic reactions under controlled conditions. Because LDH catalyzes a reversible reaction, analysis of both catalytic directions is important to define the intrinsic kinetic behavior of the enzyme and to describe the balance between substrate-, product-, and cofactor-dependent steps. The aim of this work is not to identify new *h*LDH-A inhibitors, but to establish a standardized kinetic framework to support the mechanistic interpretation of *h*LDH-A catalysis and inhibition. For this reason, selected known LDH inhibitors, namely oxamate, galloflavin, NHI-2, FX11, and gossypol, were used as benchmark compounds to evaluate how different inhibition mechanisms can be distinguished under consistent experimental conditions. Even though both directions of reaction are relevant, in the context of cancer-associated glycolytic metabolism, the pyruvate-to-lactate direction is the most relevant for inhibitor evaluation, as it directly supports NAD+ regeneration and lactate production. For this reason, the full kinetic characterization included both reaction directions, whereas the inhibitor analysis was focused on the forward reaction under controlled and physiologically relevant conditions.

A distinctive aspect of this approach is that multiple kinetic features that are commonly investigated separately, including reaction directionality, substrate and cofactor dependence, intrinsic kinetic constants, inhibition mechanism, and reaction reversibility, were considered within a single experimental and mechanistic framework. In addition, a minimal mechanistic kinetic model was developed based on experimentally determined parameters to support the interpretation of reaction reversibility and inhibitor-dependent kinetic behavior. By establishing a robust and well-defined kinetic reference framework, this work aims to provide fundamental insights into *h*LDH-A behavior and to support the future development of analytical and biosensing strategies for the biochemical evaluation of *h*LDH-A modulation under controlled in vitro conditions, possibly leading to a faster identification of potential therapeutic molecules.

2. Materials and methods

2.1. Materials

Ethanol, acetone, KH_2PO_4, K_2HPO_4, 1-hydroxy-6-phenyl-4-(trifluoromethyl)-1H-indole-2-carboxylic acid methyl ester (NHI-2), dimethylsulfoxide (DMSO), and L-lactate dehydrogenase from human (*h*LDH-A, EC 1.1.1.27) expressed in *Escherichia coli* were supplied by Sigma-Aldrich (Merck). Lactic acid, sodium pyruvate, galloflavin, NADH, and NAD were purchased from VWR Avantor. 7-Benzyl-2,3-dihydroxy-6-methyl-4-propyl-1-naphthoic acid (FX11) was provided by BLDpharm. Gossypol and oxamic acid sodium salt (oxamate) were acquired from ThermoFisher. All reagents were used as received, with no further purification.

2.2. Enzyme characterization

2.2.1. Optical analysis of reagents

All chemical species involved in the enzymatic reaction, pyruvate (substrate), NADH (reduced cofactor), NAD^+ (oxidized cofactor), and lactate (product), were analyzed by UV–Vis absorption spectroscopy to confirm the characteristic absorption peak of NADH at 340 nm [37,38]. This distinct spectral feature was subsequently employed to monitor the progress of the enzymatic reaction by tracking variations in absorbance at that specific wavelength.

In addition, the optical absorption spectra of all tested inhibitors, namely Galloflavin, NHI-2, Oxamate, Gossypol, FX11, as well as their solvent (DMSO), were independently recorded to assess any potential spectral interference with the selected analytical wavelength.

All spectra were acquired using a Jasco V-730 UV–V is spectrophotometer over a wavelength range of 225–580 nm. Measurements were performed in quartz cuvettes with a 1 cm optical path length. The analytes were dissolved in 0.1 M pH 7.4 potassium phosphate buffer and maintained at a constant temperature of 37 °C to reflect the conditions used in the subsequent kinetic assays. Potassium phosphate buffer was also used as a blank before the acquisition of the spectra.

The concentration of each compound corresponded to the maximum value employed in the enzymatic activity tests.

2.2.2. Enzyme stability tests

To ensure the reliability of the kinetic measurements, the stability of *h*LDH-A was preliminarily assessed under the adopted experimental conditions [39]. The enzyme was incubated at 37 °C for 72 h in 0.1 M pH 7.4 potassium phosphate buffer. At defined time intervals, the enzymatic activity was determined spectrophotometrically by monitoring the oxidation of NADH at 340 nm, using a Jasco V-730 instrument.

Each measurement was performed in a 2.91 mL reaction mixture containing 0.24 mM NADH and 1.69 mM pyruvate in 0.1 M pH 7.4 potassium phosphate buffer, used as a blank. The reaction was initiated by adding 100 μl of the incubated *h*LDH-A solution (0.01 mg ml^{-1}). Temperature was maintained at 37 °C throughout the measurements. Substrate and cofactor concentrations were selected based on previous literature reports [16,40], whereas the pH and temperature conditions were chosen to reflect standard physiological-like conditions typically employed in cell culture experiments.

Enzymatic activity was calculated using the eq. S1 in the Supporting Information.

All experiments were conducted in triplicate to ensure data reproducibility and to minimize the impact of random experimental error.

2.2.3. Kinetic evaluation of the forward and reverse reaction in physiological-like conditions

The kinetic behavior of *h*LDH-A was investigated under steady-state conditions by analyzing both the forward (pyruvate-to-lactate) and reverse (lactate-to-pyruvate) reactions, in order to determine the intrinsic kinetic parameters of the enzyme.

Kinetic tests were performed using a Jasco V-730 UV–Vis spectrophotometer. The reaction progress was followed by monitoring the oxidation of NADH at 340 nm. All assays were conducted at 37 °C in 0.1 M pH 7.4 potassium phosphate buffer, with a final reaction volume of 3.01 mL. Enzyme concentration and assay conditions were selected to ensure linear initial reaction rates and negligible substrate depletion.

For the forward reaction, kinetic curves were obtained by varying pyruvate concentration from 0 to 1 mM inside the cuvette, while keeping NADH at fixed concentrations. Specifically, four independent kinetic curves were recorded, each corresponding to a different NADH concentration. In a complementary set of experiments, NADH concentration was varied from 0 to 0.3 mM, while maintaining pyruvate at fixed levels.

An analogous experimental design was adopted for the reverse reaction, in which lactate and NAD^+ concentrations were systematically varied, from 0 to 0.6 mM or 0 to 0.3 mM, respectively.

For each substrate–cofactor concentration pair, the initial reaction rate, used to construct the corresponding kinetic curves, was calculated from the linear portion of the absorbance–time traces using Eq. (S1).

Each kinetic dataset was initially fitted using the Michaelis–Menten model to obtain apparent kinetic parameters. Linearization according to the Hanes–Woolf method was subsequently employed to improve robustness against experimental error relative to the Lineweaver–Burk approach [41]. The equations used for kinetic fitting and linearization, together with the definition of all kinetic parameters, are reported in the Supporting Information (Eq. S2–S3). To avoid relying exclusively on a linearized form of the kinetic equation, the original untransformed data were also analyzed by nonlinear least-squares fitting [42]. The same kinetic model was applied in both analyses, and nonlinear regression was used to validate the parameters obtained from the Hanes–Woolf representation. Hanes–Woolf plots were retained as a graphical and comparative tool because they allow clear visualization of trends in apparent kinetic parameters and inhibition patterns; however, the limitations associated with linearization, including potential distortion of error structure and altered weighting of data points, were taken into account in the interpretation of the results.

The intrinsic kinetic parameters of *h*LDH-A were then determined, within a kinetic framework consistent with an ordered sequential bi–bi mechanism, in which the binding of the cofactor precedes that of the substrate. This binding sequence is due to a cofactor-induced conformational change essential for the subsequent docking of the substrate.

Under steady-state conditions, the initial reaction rate is described by the Cleland equation (Supporting Information, Eq. (S4)) [43–46]. To this end, secondary plots were constructed from the apparent kinetic parameters obtained at different fixed concentrations of the second substrate or cofactor. Analysis of these plots enabled the extraction of the intrinsic kinetic constants for both the forward and reverse reactions [11,47] as detailed in the Supporting Information.

After the determination of the intrinsic maximum velocity, both for the forward and reverse reactions, the turnover number (k_{cat}) was evaluated according to eq. S5 of the Supporting Information.

All experiments were carried out in triplicate to ensure reproducibility.

2.2.4. Inhibitors evaluation

To evaluate the effect of selected inhibitors on *h*LDH-A activity, kinetic assays focused on the forward reaction were conducted. All measurements were performed by monitoring the decrease in absorbance at 340 nm, using a Jasco V-730 spectrophotometer. The reaction mixture, kept at 37 °C, contained NADH and pyruvate at the specified concentrations and the inhibitor under examination. To ensure system homogeneity, the mixture was maintained under constant magnetic stirring throughout the experiments. For each assay condition, the corresponding blank solution contained phosphate buffer, NADH, pyruvate, solvent, and inhibitor at the same concentrations used in the reaction mixture, but without enzyme. This enzyme-free blank was used for baseline correction before initiating the reaction. Reactions were initiated by adding 100 μL of *h*LDH-A solution (0.01 mg mL^{-1}) to the pre-equilibrated blank solution.

A complete kinetic profile was established by systematically varying substrate and cofactor concentrations, following the experimental design used for the uninhibited enzyme. In pyruvate-dependent assays, pyruvate concentration was varied in the range 0.005–1 mM while NADH concentration was kept constant at 0.23 mM. Conversely, in NADH-dependent assays, pyruvate concentration was fixed at 1.63 mM, and NADH concentration ranged from 0.005 to 0.30 mM. These concentration ranges were selected to avoid signal saturation and ensure accurate determination of initial reaction rates.

For inhibition assays, five different concentrations were tested for each compound. Galloflavin and FX11 were evaluated within a concentration range of 1–20 μM, whereas all other inhibitors were tested between 1 and 40 μM.

Except for oxamate, which was solubilized in deionized water, all other inhibitors were dissolved in DMSO. To assess potential solvent-related effects on *h*LDH-A activity, control assays were performed at varying DMSO concentrations ranging from 0.04% to 5% (*v*/v), exceeding the maximum solvent concentration introduced during inhibition experiments. This control ensured that any observed changes in enzymatic activity could be attributed to inhibitor action rather than to solvent interference.

Absorbance data were converted into initial reaction rates using Eq. S1 reported in the SI. Apparent kinetic parameters were calculated using the Hanes–Woolf linearization method [48]. Since the inhibitors were not consumed during the enzymatic assay, their absorbance contribution at 340 nm was treated as a constant baseline component. Therefore, the use of inhibitor-containing enzyme-free blanks allowed this contribution to be corrected before evaluating the time-dependent NADH decrease.

Inhibition patterns were assigned based on the combined evaluation of Hanes–Woolf linearizations, Michaelis–Menten kinetic curves, and inhibitor-dependent changes in the apparent kinetic parameters. Variations in slope, y-intercept, and x-intercept of the Hanes–Woolf plots were used to distinguish apparent competitive, non-competitive, and mixed-type behaviors under the tested assay conditions. For selected

diagnostically relevant cases, ANOVA-based comparisons of the linear regressions were performed to evaluate whether changes in regression parameters were statistically significant. These analyses were used as supporting evidence for kinetic interpretation, which remains valid under the tested conditions, and were not intended to replace a comprehensive global inhibition model-selection procedure.

Three-dimensional structures of *h*LDH-A, the reaction substrates and products, and the tested inhibitors were visualized using UCSF Chimera, version 1.18. The crystallographic structure of *h*LDH-A was retrieved from UniProt data bank (UniProt ID. K1T0A2) [49]. Molecular structures of pyruvate, NADH, and the investigated inhibitors (oxamate, galloflavin, NHI-2, gossypol, and FX11) were obtained from PubChem and rendered for visualization purposes [50].

UCSF Chimera was also used to visualize results of molecular docking analysis, performed with AutoDock Vina. Docking was used to investigate the possible binding orientation of the tested inhibitors within the *h*LDH-A catalytic region. Computational analyses were carried out for each ligand individually. The enzyme structure was prepared by removing non-essential molecules, adding hydrogen atoms, and optimizing the receptor for ligand docking. Subsequently, ligands were docked in their minimum energy conformation, and exploratory structure analysis was implemented to identify hydrogen bonds between the ligand and the enzyme's amino acid residues. Representative docking poses were selected based on docking score and visual inspection of their localization within the enzymatic pocket.

The docking analysis was intended to provide qualitative structural support to the kinetic results. Therefore, docking poses were interpreted in combination with the experimentally determined inhibition profiles rather than used as standalone evidence for mechanistic assignment.

2.2.5. Determination of inhibition constants

Inhibition constants (K_i) were determined exclusively for the forward reaction under pyruvate-variation conditions, since the pyruvate-to-lactate conversion catalyzed by *h*LDH-A represents the physiologically predominant direction supporting NAD^+ regeneration and sustained glycolytic flux, particularly in highly glycolytic contexts [51,52]. Moreover, performing K_i analysis by varying pyruvate at fixed NADH minimized additional kinetic complexity associated with cofactor-dependent steps in the ordered sequential bi–bi mechanism. In addition, this configuration was selected because the pyruvate-to-lactate direction is directly linked to NAD+ regeneration and lactate production in highly glycolytic contexts. NADH-variation experiments were used as complementary kinetic information to identify possible cofactor-dependent effects, whereas the quantitative comparison of inhibitor potency was restricted to a single pyruvate-variable assay configuration.

K_i values were extracted through secondary plot analysis, based on the apparent kinetic parameters obtained from the Hanes-Woolf linearizations. The mathematical form of these plots depended on the identified inhibition mechanism [47]. Specifically, in the case of competitive inhibition, the apparent Michaelis constant (K_M^{app}) was plotted as a function of inhibitor concentration ([I]). For non-competitive inhibition, the reciprocal apparent maximum velocity ($1/R_{p,max}^{app}$) was plotted versus the inhibitor concentration. Lastly, for mixed-type inhibition, the ratio $K_M^{app}/R_{p,max}^{app}$ was plotted against inhibitor concentration. In all three cases, the K_i values were determined from the x-intercept of the corresponding linear regression.

K_i values are reported as mean ± standard deviation. Goodness-of-fit was assessed using the coefficient of determination (R^2). Where appropriate, fitted parameters were reported together with uncertainty estimates. Moreover, where necessary, an ANOVA test was performed to assess the statistical difference between data.

2.3. Reaction modeling

The LDH-A-catalyzed reaction was modeled using a reversible ordered sequential bi-bi mechanism (Eq. 1). In Eq. 1, E represents the enzyme, A is NADH, B is pyruvate, P is lactate, and Q is NAD^+.

$$E + A + B \underset{k_{-1}}{\overset{k_1}{\rightleftharpoons}} EA + B \underset{k_{-2}}{\overset{k_2}{\rightleftharpoons}} EAB (\rightleftharpoons EPQ) \underset{k_{-3}}{\overset{k_3}{\rightleftharpoons}} EQ + P \underset{k_{-4}}{\overset{k_4}{\rightleftharpoons}} E + Q + P \quad (1)$$

From Eq. 1, the net velocity of the reaction was obtained, with all the intermediate steps provided in Eqs. S6-S13. This derivation yielded a system of ordinary differential equations that govern the time-dependent concentration profile of all the species involved in the reaction. To improve the representativeness of the model, a term accounting for thermal inactivation of the enzyme was integrated. The full set of equations that describes the system is detailed in Eq. 2.

$$\begin{cases} v(t) = \dfrac{k_{cat,f} \bullet [e] \bullet \dfrac{[A] \bullet [B]}{K_{ia} \bullet K_b} - k_{cat,r} \bullet [e] \bullet \dfrac{[P] \bullet [Q]}{K_{iq} \bullet K_p}}{1 + \dfrac{[A]}{K_{ia}} + \dfrac{K_a \bullet [B]}{K_{ia} \bullet K_b} + \dfrac{[A] \bullet [B]}{K_{ia} \bullet K_b} + \dfrac{[Q]}{K_{iq}} + \dfrac{K_q \bullet [P]}{K_{iq} \bullet K_p} + \dfrac{[P] \bullet [Q]}{K_{iq} \bullet K_p}} \\ \dfrac{d[A]}{dt} = -v(t) \\ \dfrac{d[B]}{dt} = -v(t) \\ \dfrac{d[P]}{dt} = v(t) \\ \dfrac{d[Q]}{dt} = v(t) \\ \dfrac{d[e]}{dt} = -k_d \bullet [e] \end{cases} \quad (2)$$

The model was formulated as a minimal reversible mechanistic framework based on the experimentally determined kinetic parameters. Enzyme aggregation was not explicitly included, because the enzyme concentration used in the kinetic and validation experiments was very low and the reaction times were short compared with the time scale of the stability assay, making aggregation-related effects unlikely to dominate under the adopted conditions. Nevertheless, since no direct structural or scattering-based analysis of aggregation was performed, this process cannot be fully excluded and is acknowledged as a possible limitation.

Dynamic conformational states were also not explicitly modeled. Although conformational changes are known to contribute to the catalytic behavior of LDH and other NAD-dependent dehydrogenases, their reliable incorporation into a kinetic model would require independent experimental information, such as pre-steady-state kinetic data, binding kinetics, or time-resolved structural evidence. In the absence of such constraints, introducing additional conformational states would increase the number of poorly identifiable parameters and could lead to overparameterization. Therefore, conformational effects were implicitly included in the experimentally estimated kinetic parameters, while the final model was retained as a minimal framework aimed at describing the dominant kinetic behavior under the tested conditions.

Two different types of inhibition were also modeled, namely competitive and non-competitive inhibition. In both cases, inhibition was incorporated by adding the corresponding terms to the denominator of the net rate equation. Competitive inhibition was modeled by adding a term for the competition between the inhibitor and pyruvate for the same binding site, leading to the modified net velocity described in the following equation.

$$v(t) = \frac{k_{cat,f} \bullet [e] \bullet \frac{[A] \bullet [B]}{K_{ia} \bullet K_b} - k_{cat,r} \bullet [e] \bullet \frac{[P] \bullet [Q]}{K_{iq} \bullet K_p}}{1 + \frac{[A]}{K_{ia}} + \frac{K_a \bullet [B]}{K_{ia} \bullet K_b} + \frac{[A] \bullet [B]}{K_{ia} \bullet K_b} + \frac{[Q]}{K_{iq}} + \frac{K_q \bullet [P]}{K_{iq} \bullet K_p} + \frac{[P] \bullet [Q]}{K_{iq} \bullet K_p} + \frac{K_a \bullet [B] \bullet [I]}{K_{ia} \bullet K_c \bullet K_i}} \quad (3)$$

For non-competitive inhibition, the whole denominator is multiplied by a factor greater than one to model the reduction in the effective catalytic activity of the enzyme without the alteration of substrate binding affinities. In this case, the net reaction velocity becomes:

$$v(t) = \frac{k_{cat,f} \bullet [e] \bullet \frac{[A]\bullet[B]}{K_{ia}\bullet K_b} - k_{cat,r} \bullet [e] \bullet \frac{[P]\bullet[Q]}{K_{iq}\bullet K_p}}{\left(1 + \frac{[A]}{K_{ia}} + \frac{K_a\bullet[B]}{K_{ia}\bullet K_b} + \frac{[A]\bullet[B]}{K_{ia}\bullet K_b} + \frac{[Q]}{K_{iq}} + \frac{K_q\bullet[P]}{K_{iq}\bullet K_p} + \frac{[P]\bullet[Q]}{K_{iq}\bullet K_p}\right) \bullet \left(1 + \frac{[I]}{K_i}\right)} \quad (4)$$

All kinetic parameters used in the model were experimentally determined, as detailed in the previous sections. In simulations involving inhibition, the K_i value for competitive inhibition was based on the value determined for oxamate, whereas the K_i for non-competitive inhibition was derived from the value obtained for FX11. The set of differential equations has been solved using MATLAB® and Simulink. More specifically, the block diagram used to describe and solve the differential equations has been created with Simulink, while MATLAB® has been used to set up the initial conditions for the ODE and analyse the results, comparing them with the experimental data. The system of differential equations was solved by numerical integration [53], using the Simulink solver. The solver was configured with a variable-step method and a maximum step size of 0.001 to ensure adequate resolution.

2.4. Model validation

The predictive capability of the proposed kinetic model was assessed through independent validation experiments, performed at 37 °C in 0.1 M pH 7.4 phosphate buffer, with equal initial concentrations of NADH and pyruvate. These concentrations were selected to ensure a sufficiently slow reaction rate, enabling reliable time-resolved monitoring of NADH consumption. The enzyme concentration was selected according to the same criteria and was kept constant throughout the experiments. At predetermined time intervals, aliquots of 3 mL were withdrawn from the reaction mixture. Enzymatic activity was immediately quenched by the addition of 3 mL of 0.1 M HCl, ensuring complete enzyme inactivation and preventing further reaction progress.

The residual NADH concentration was determined spectrophotometrically by measuring the absorbance at 340 nm. Quantification was performed using a calibration curve relating absorbance to NADH concentration, as described in the Supporting Information.

All experiments were conducted in triplicate to ensure reproducibility. The experimentally obtained NADH concentration profiles were subsequently compared with model predictions generated by numerical solutions of the kinetic equations described in Section 2.3. The coefficient of determination (R^2) and the relative prediction error were used to assess the agreement between experimental and simulated values.

These validation experiments were not intended to provide exhaustive assessment over a broad experimental space, but rather to test whether the mechanistic model could reproduce the NADH consumption profile under simple and controlled conditions.

3. Results and discussion

3.1. Optical validation of NADH-based spectrophotometric monitoring

The UV–Vis absorption spectra of all chemical species involved in the reaction mixture are shown in Fig. 1 and are reported as absorbance values in arbitrary units.

NAD^+ and NADH displayed a characteristic absorption band in the ultraviolet region around 260 nm, which is attributed to π → π* transitions of adenine, common to both cofactors. Moreover, NADH exhibited a well-defined absorption band centered at 340 nm, which was absent in the spectra of NAD^+, and arises from π → π* transitions of the reduced nicotinamide ring [54]. In contrast, pyruvate showed only weak absorption features confined to the lower ultraviolet region, resulting in negligible absorbance contributions at the analytical wavelength used for kinetic measurements. Lactate displayed an absorption band centered at 280 nm, which was largely masked by the overlapping signal of NAD^+. As a result, enzymatic reactions involving NADH-dependent dehydrogenases are commonly monitored by measuring absorbance changes at 340 nm, which reflect NADH consumption stoichiometrically coupled to pyruvate reduction and concomitant lactate and NAD^+ formation [38,54,55].

The validity of this approach relies on the assumption that no other reagents or products contribute time-dependent absorbance variations at the analytical wavelength. In this context, the absorption spectra of the solvent (DMSO) and of the tested inhibitors were also examined. Most inhibitors exhibited minimal absorbance at 340 nm at the concentrations employed in the kinetic assays. In contrast, NHI-2 showed a measurable absorbance contribution at this wavelength, leading to a higher initial absorbance value in solutions containing this compound. Importantly, the absorbance associated with NHI-2 remained constant over the time scale of the enzymatic assays, indicating that the inhibitor

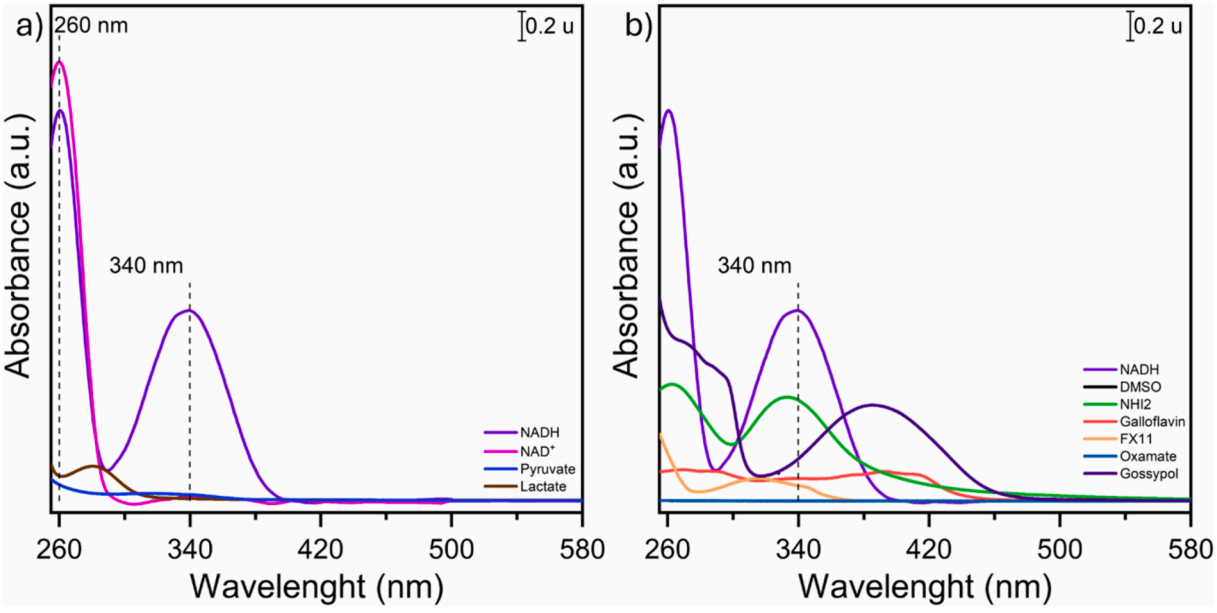

Fig. 1. UV absorption spectra of a) 0.23 mM NAD+, 0.23 mM NADH, 1.63 mM lactate, 1.63 mM pyruvate; b) 0.23 mM NADH, 9.49 mM DMSO, 40 μM NHI-2, 20 μM galloflavin, 20 μM FX11, 40 μM Oxamate and 40 μM Gossypol.

was not consumed or chemically modified during the reaction.

As enzymatic activity was determined from the time-dependent change in absorbance rather than from absolute absorbance values, the presence of a constant absorbance offset did not affect the determination of initial reaction rates [56,57]. Accordingly, variations in absorbance at 340 nm could be reliably attributed to NADH oxidation, both in the absence and in the presence of inhibitors.

3.2. *h*LDH-A thermal stability

The thermal stability of *h*LDH-A under physiological-like conditions was evaluated by monitoring the residual enzymatic activity following incubation at 37 °C in phosphate buffer (pH 7.4) over an extended time period, as reported in Fig. 2. Enzymatic activity values were normalized to the initial activity measured at time zero and expressed as percentage residual activity.

The experimental activity–time profile was quantitatively described using a first-order deactivation model, according to the following equation [47]:

$$A(t) = A_0 \bullet e^{-k_D t} \tag{5}$$

where A(t) represents the residual enzymatic activity at time t, A_0 is the initial activity, and $k_D$is the first-order inactivation constant (h^{-1}). This model was selected as a simple phenomenological description of the decrease in residual catalytic activity over time, rather than as a mechanistic representation of the molecular events responsible for enzyme deactivation. The fitting provided a good empirical description of the experimental data, with an R^2 value of 0.97, supporting its use to describe the apparent activity decay under the tested conditions.

Fitting the experimental data to this model resulted in an inactivation constant $k_D = 0.02316\ h^{-1}$, indicating a gradual loss of enzymatic activity over time.

From the estimated deactivation constant, the half-life of enzymatic activity ($t_{1/2}$) was calculated, yielding a value of approximately 30 h. As shown in Fig. 2, *h*LDH-A retained a substantial fraction of its catalytic activity during the early incubation period, followed by a progressive decrease upon prolonged exposure to the tested temperature. After 72 h of incubation, approximately 20–25% of the initial activity was still preserved.

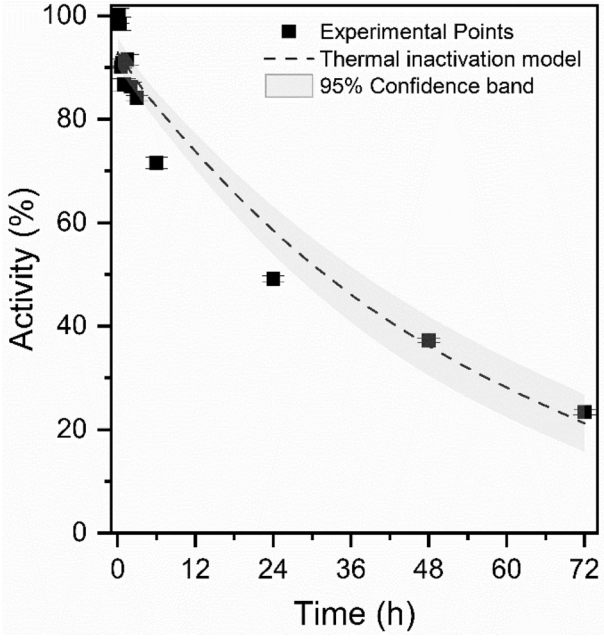

Fig. 2. Thermal inactivation of hLDH-A under physiological-like conditions. The enzymatic solution was incubated at pH 7.4 and 37 °C. Residual activity was normalized to the initial activity measured at time zero.

The purpose of this experiment was to assess whether *h*LDH-A retained sufficient catalytic activity over time scales relevant to the kinetic assays. Indeed, the kinetic measurements were performed over substantially shorter time intervals than the 72 h incubation used for the stability test. In addition, the enzyme concentration was kept sufficiently low to minimize aggregation-related effects under the adopted experimental conditions. However, because no direct structural analysis of protein unfolding, aggregation, or irreversible denaturation was performed, the observed decrease in activity should be interpreted as an apparent loss of catalytic function rather than as evidence for a specific thermal deactivation mechanism.

Overall, these results indicate that *h*LDH-A undergoes slow thermal deactivation under physiological-like conditions, while maintaining sufficient stability over time scales relevant to kinetic assays. This behavior supports the reliability of the enzymatic measurements reported in this study, since none of the assays required enzyme exposure at 37 °C for more than two hours, and highlights the importance of accounting for enzyme stability in long-term kinetic investigations. Thermal inactivation of enzymes can generally result from different molecular processes, including partial or complete unfolding and aggregation, both of which may reduce the fraction of catalytically active enzymes. In the present study, these processes were not investigated separately by structural or aggregation-specific techniques. Instead, thermal stability was evaluated functionally by monitoring the residual enzymatic activity over time. Therefore, the measured activity decay should be interpreted as the overall apparent consequence of the thermal inactivation processes rather than as evidence of a specific molecular pathway.

3.3. Mechanistic kinetic analysis of hLDH-A

Before the comprehensive kinetic analysis, the suitability of different linearization approaches for the determination of apparent kinetic parameters was evaluated. Representative kinetic curves obtained by varying substrate concentration at fixed cofactor levels were analyzed using both Lineweaver–Burk (LB) and Hanes–Woolf (HW) representations. Fig. 3 reports the experimental points fitted with HW linearization, while the graphical comparison between the two methods is reported in Fig. S1.

Hanes-Woolf linearization was found to provide an adequate representation of the experimental points both for the forward and the reverse reactions, as shown in Fig. 3. Fig. S1 provides better insight into the comparison between the two methods. Although both methods provide linear transformations of the Michaelis–Menten equation, substantial differences in fitting quality were observed, particularly for pyruvate-dependent kinetics. These differences can be mainly attributed to the different propagation of experimental errors in the two transformations [58]. In the Lineweaver–Burk representation, the reciprocal transformation disproportionately amplifies experimental uncertainty associated with data points collected at low substrate concentrations, as small absolute errors in reaction rate translate into large deviations upon inversion. In fact, assuming that experimental errors in the measured reaction rate are approximately constant in absolute terms, first-order error propagation shows that the transformed error is presented in Eq. 6.

$$\varepsilon^{LB} \approx -\frac{\varepsilon_{R_p}}{R_p^2} \tag{6}$$

Therefore, at low substrate concentrations, where R_p is proportional to [S], the transformed error is proportional to $1/[S]^2$, leading to marked heteroscedasticity and high leverage of low [S] data points [59,60]. As a result, these points may disproportionately influence parameter estimation and lead to poorer representation of the full dataset [11,61]. This effect is especially pronounced for pyruvate-dependent kinetics, where deviations from ideal Michaelis–Menten behavior are observed at both

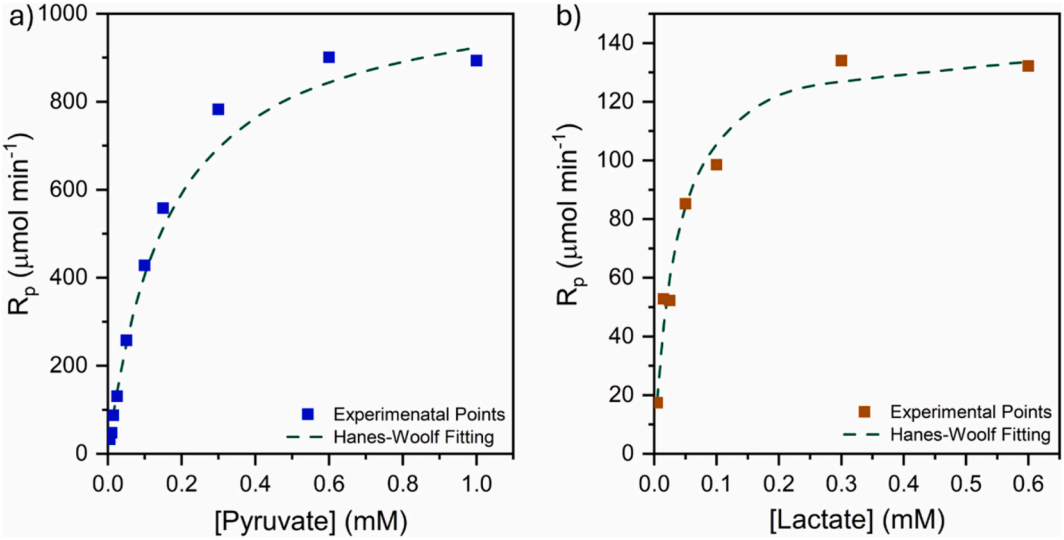

Fig. 3. Kinetic characterization of the LDH-catalyzed reaction. Reaction rates were measured as a function of pyruvate (a) or lactate (b) concentration. Symbols indicate experimental data, while dashed lines correspond to nonlinear fits derived from HW linearization approach. Both substrates exhibit a hyperbolic dependence of reaction rate on concentration, consistent with Michaelis–Menten kinetics.

low and high substrate concentrations.

In contrast, the Hanes–Woolf transformation modifies the error structure more moderately. Error propagation indicates that the transformed error scales approximately as shown in Eq. 7.

$$\varepsilon^{HW} \approx -\frac{[S] \bullet \varepsilon_{R_p}}{R_p^2} \tag{7}$$

For low substrate concentrations, the Michaelis-Menten equation can be approximated as

$$R_p \approx \frac{R_{p,max}}{K_M} \bullet [S] \tag{8}$$

Therefore, $\varepsilon^{HW} \sim 1/[S]$. This represents a weaker divergence at low substrate concentrations. Moreover, because the independent variable remains proportional to substrate concentration, statistical leverage is more evenly distributed across the dataset. As a result, experimental error is distributed more uniformly along the regression line, leading to kinetic parameters that better reproduce the experimental data. This behavior is consistent with previous methodological analyses highlighting the superior robustness of the Hanes–Woolf approach in the presence of experimental noise and non-ideal kinetic features [11,61–63]. On this basis, the Hanes–Woolf method was selected for the determination of apparent kinetic parameters throughout this study.

The steady-state kinetics of *h*LDH-A for the forward reaction were investigated by independently varying NADH concentration at fixed pyruvate levels and pyruvate concentration at fixed NADH levels (Fig. 4). In all cases, the experimental data displayed trends consistent with Michaelis–Menten-type behavior.

Apparent kinetic parameters derived from Hanes–Woolf linearization under all experimental conditions are reported in Table S1. For comparison, Table S1 also reports the corresponding kinetic parameters obtained by nonlinear least-squares regression of the untransformed data, allowing a direct quantitative assessment of the agreement between the two approaches. Overall, nonlinear regression provided parameter estimates in good agreement with those derived from

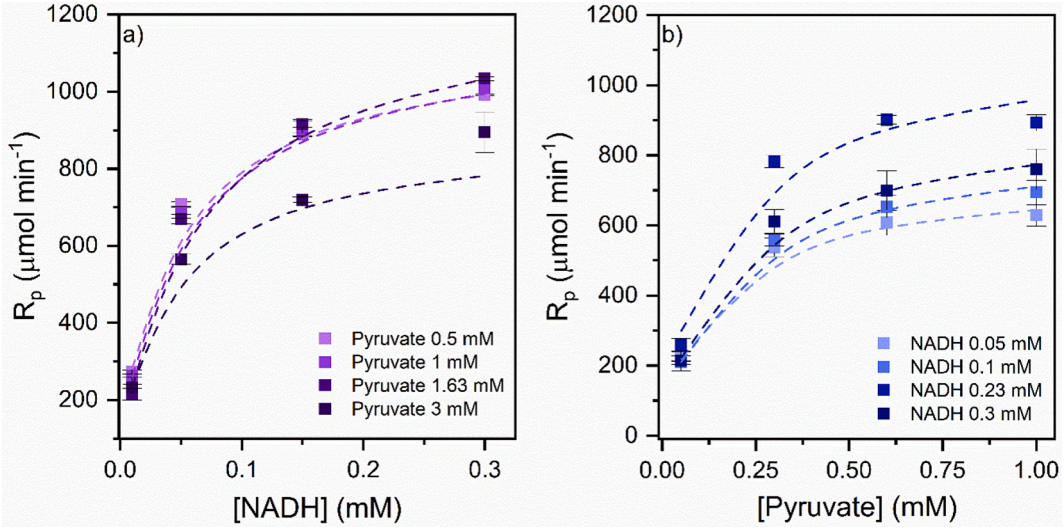

Fig. 4. Kinetic analysis of the LDH-catalyzed forward reaction as a function of (a) NADH concentration at increasing fixed pyruvate concentrations and (b) pyruvate concentration at increasing fixed NADH concentrations. Symbols represent mean values ± standard deviation from triplicate measurements, while dashed lines indicate Michaelis–Menten fits.

Hanes–Woolf analysis. Under all investigated conditions, the Hanes–Woolf-derived estimates fell within the corresponding 95% confidence intervals of the nonlinear-regression parameters. Relative differences between the two approaches were generally limited, although larger deviations were observed at the highest fixed pyruvate concentration (3 mM), for which the nonlinear estimates were also associated with wider confidence intervals. These results support the use of the Hanes–Woolf representation for graphical and comparative purposes while providing an independent quantitative validation based on direct fitting of the untransformed data.

Notably, variations in NADH concentration produced more pronounced changes in the kinetic profiles compared to variations in pyruvate concentration. Increasing NADH levels up to 0.23 mM resulted in a substantial increase in apparent reaction rates (Fig. 4b), followed by a decrease at higher cofactor concentration, suggesting a reduced catalytic efficiency at elevated NADH levels. The apparent Michaelis constant for NADH (K_M^{app}) showed moderate variations across the investigated concentration range. Taking the value obtained at 0.23 mM NADH as a reference, deviations remained within 15%, with the largest difference observed at 0.05 mM NADH (15%), followed by 14% at the highest concentration examined and 8.6% at 0.1 mM NADH.

Conversely, changes in pyruvate concentration induced smaller effects (Fig. 4a). No substantial variation in the apparent maximum velocity was observed, while the apparent Michaelis constant varied as a function of NADH, reflecting the coupling between substrate and cofactor binding typical of bi-substrate enzymes.

This observation suggests a dominant influence of the cofactor on enzymatic activity, compatible with a cofactor-first ordered sequential mechanism, as previously reported for lactate dehydrogenase and other NAD-dependent dehydrogenases [45,64–66].

At elevated pyruvate concentrations, a reduction in the apparent maximum reaction rate was observed, suggesting the onset of substrate inhibition. This behavior may reflect the formation of non-productive enzyme–substrate complexes or allosteric effects at high substrate levels, a phenomenon commonly reported for LDH and other enzymes operating at high metabolite concentrations [20,67–69].

An analogous kinetic analysis was performed for the reverse reaction by varying lactate concentration at fixed NAD^+ levels (Fig. S2 a) and NAD^+ concentration at fixed lactate levels (Fig. S2 b). The apparent kinetic parameters obtained from both Hanes–Woolf analysis and direct nonlinear least-squares regression are reported in Table S2. Overall, nonlinear regression reproduced the general magnitude and trends of the Hanes–Woolf-derived parameters, although the agreement was less uniform than that observed for the forward reaction. Most Hanes–Woolf estimates fell within the corresponding 95% confidence intervals of the nonlinear fits, while larger deviations were observed under selected fixed-lactate conditions, particularly at 0.5 and 3 mM. This greater variability is consistent with the reduced robustness of the kinetic description previously observed for the reverse reaction.

As observed for the forward reaction, variations in cofactor concentration exerted a stronger influence on enzymatic activity than variations in substrate concentration, suggesting a cofactor-first ordered sequential mechanism for interpreting the kinetic data [45,46,70]. In fact, increasing NAD^+ concentration led to a progressive increase in the apparent reaction rate, which may reflect a strong dependence of the reverse reaction on cofactor availability.

Conversely, when lactate is the varied substrate, the apparent maximum reaction rate increased up to intermediate lactate levels, followed by a reduction at elevated concentrations, indicating the onset of substrate inhibition analogous to that observed for pyruvate [71].

Overall, the dependence of the apparent kinetic parameters on the concentration of the second reactant highlights the intrinsic limitations of apparent kinetic analysis for mechanistic interpretation. For this reason, intrinsic kinetic parameters were determined through secondary plot analysis, assuming an ordered sequential bi-bi mechanism, consistent with the previous observations and supported by literature.

For the forward reaction, secondary plots derived from the apparent kinetic parameters obtained at varying NADH concentrations exhibited linear trends (Fig. 5 a and b), compatible with the assumptions of an ordered sequential mechanism [11,72]. From these plots, the intrinsic kinetic parameters $R_{p,max}$, K_A, K_B, and K_{iA} were determined, according to the procedure described in the Supporting Information, and are summarized in Table 1.

An analogous secondary plot analysis was reported for the reverse reaction by varying NAD^+ and lactate concentrations (Fig. 5 c and d). In this case, the linear relationships were less pronounced than those observed for the forward reaction, suggesting a reduced robustness of the kinetic description in the lactate-to-pyruvate direction. This behavior is consistent with the lower catalytic efficiency observed for the reverse reaction under the investigated conditions [73]. The corresponding intrinsic kinetic parameters are also reported in Table 1.

Comparison of the estimated parameters indicated a markedly higher catalytic throughput for the pyruvate-to-lactate reaction under the tested physiological-like conditions. Although the substrate-related parameters suggest stronger apparent affinity toward lactate, the higher forward reaction rate indicates that substrate affinity alone is not sufficient to explain the observed direction-dependent kinetic behavior [74]. Within the adopted ordered sequential bi–bi framework, this behavior is compatible with an important contribution of catalytic turnover and cofactor-dependent steps to the overall hLDH-A kinetic response [74–78].

Therefore, the observed catalytic asymmetry should be interpreted as a condition-dependent kinetic feature of hLDH-A within the experimental and modeling assumptions used in this study, rather than as definitive proof of a unique molecular mechanism governing reaction directionality. [28,74–79]

3.4. Evaluation of inhibitory effects

Once a detailed understanding of the intrinsic kinetic behavior of *h*LDH-A was established, reference inhibitors were subsequently investigated. Kinetic analyses were performed exclusively on the forward reaction, as it represents the physiologically favored direction and the catalytically relevant process in cancer cell metabolism.

Prior to inhibitor evaluation, the potential influence of the solvent on *h*LDH-A catalytic activity was assessed. To this end, kinetic assays were performed in the presence of increasing concentrations of DMSO, covering and exceeding the maximum solvent content employed in inhibition experiments. In these assays, kinetic curves were constructed by independently varying pyruvate (keeping NADH at a constant concentration of 0.23 mM) or NADH concentration (with pyruvate concentration fixed at 1.63 mM). Representative kinetic curves obtained at different DMSO concentrations are reported in Fig. S3.

Overall, the reaction rates exhibited comparable trends across the investigated solvent concentrations, both under variable pyruvate and NADH conditions, with no systematic dependence on DMSO content. Although minor variations in the absolute reaction rates were observed among individual curves, especially in pyruvate-dependent assays, these variations did not follow a concentration-dependent pattern and remained within the experimental variability of the assay.

On this basis, DMSO was not found to exert a significant or systematic effect on *h*LDH-A kinetic behavior under the adopted experimental conditions. Consequently, any changes in enzymatic activity observed in the presence of inhibitors can be reasonably attributed to inhibitor–enzyme interactions rather than to solvent-related effects.

A panel of LDH inhibitors previously reported in the literature, including galloflavin, NHI-2, oxamate, FX11, and gossypol, was therefore evaluated to assess their impact on the kinetic behavior of *h*LDH-A.

The inhibition mechanisms discussed below should be interpreted as apparent kinetic patterns under the specific assay configurations used in this study. Mechanistic assignment was based on the combined

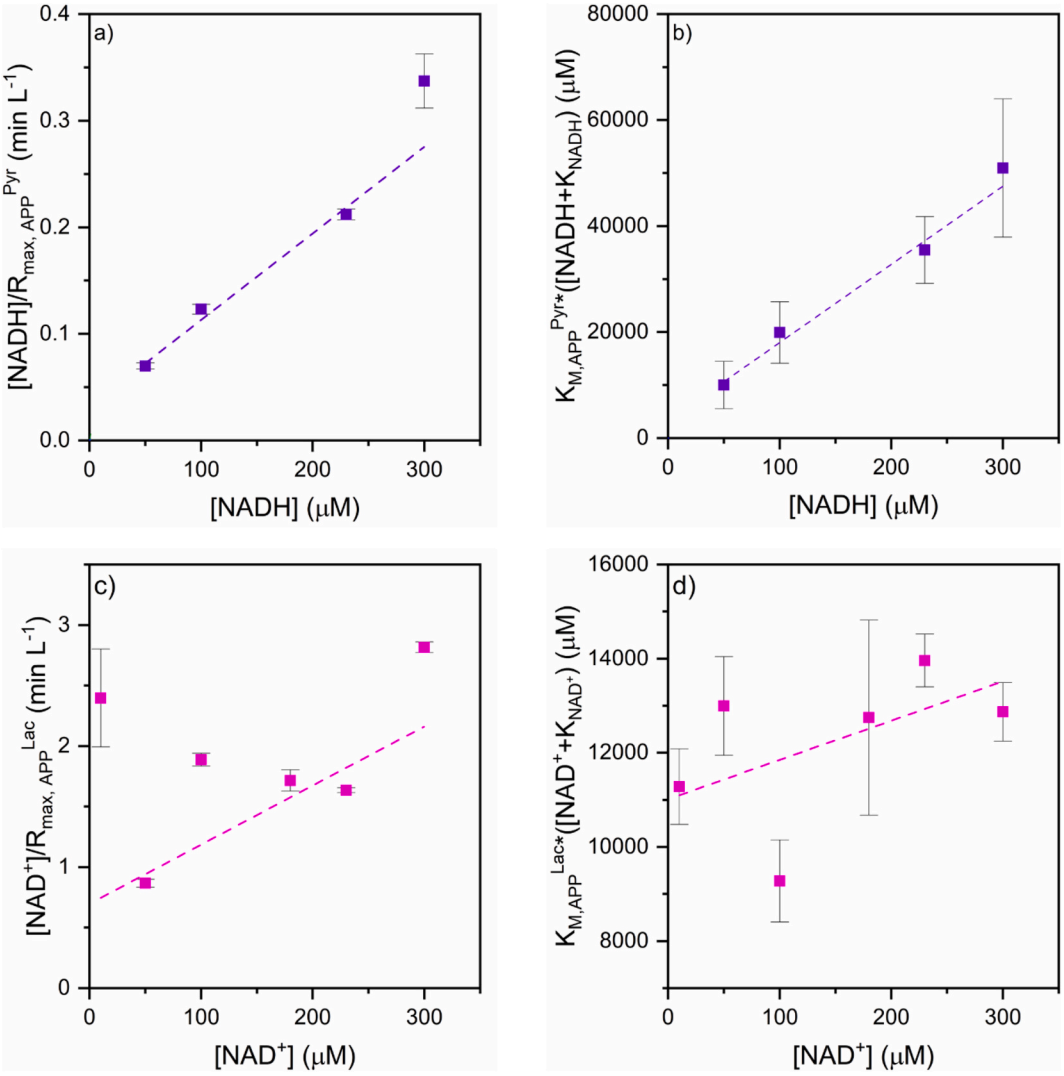

Fig. 5. (a and b) Secondary plots derived from the apparent kinetic parameters obtained for the forward reaction by varying NADH concentration at fixed pyruvate levels. (c and d) Secondary plots derived from the apparent kinetic parameters obtained for the reverse reaction by varying NAD^+ concentration at fixed lactate levels. Data points represent mean values ± standard deviation obtained from triplicate measurements. Dashed lines indicate linear fits used to extract the intrinsic kinetic parameters ($R_{p,max}$, K_A, K_B, and K_{iA}) within the adopted ordered sequential reaction mechanism. Details of the kinetic model and fitting procedure are reported in the Supporting Information.

Table 1
Intrinsic kinetic parameters for the forward and the reverse reactions.

Reaction direction	$R_{p,max}$ (μmol min^{-1})	K_A (mM)	K_B (mM)	K_{iA} (mM)	k_{cat} (s^{-1})
Forward[(a)]	1230.7 ± 46.9	0.039 ± 0.005	0.15 ± 0.04	0.02 ± 0.01	769.2
Reverse[(b)]	204.5 ± 74	0.142 ± 0.009	0.009 ± 0.003	0.222 ± 0.09	127.8

(a) In the forward reaction, A refers to NADH, B to pyruvate
(b) In the reverse reaction, A refers to NAD+, B to lactate

inspection of Hanes–Woolf plots, Michaelis–Menten curves, and the corresponding changes in apparent kinetic parameters. For inhibitors displaying concentration-dependent changes or different behavior depending on the varied ligand, the assigned mechanism represents the predominant kinetic pattern observed under the tested conditions rather than an exhaustive description of all possible inhibitor-bound enzyme states.

To elucidate the inhibition mechanisms of the selected compounds, kinetic data were analyzed using Hanes–Woolf linearization, which allows discrimination between competitive, non-competitive, and mixed inhibition based on changes in slope and intercept. In Hanes–Woolf representations, changes in slope are primarily associated with variations in the apparent Michaelis constant, whereas changes in the intercept reflect variations in the apparent maximum velocity. Parallel lines indicate competitive inhibition, while intersecting lines are indicative of non-competitive or mixed inhibition mechanisms, depending on the position of the intersection [11,80,81]. Results for oxamate and gallo-flavin are reported in Fig. 6 and Fig. 7, respectively, while the complete linearization set is shown in Fig. S6.

The interpretation of these plots was supported by inspection of the corresponding Michaelis–Menten kinetic curves, reported in the Supporting Information (Fig. S4 and Fig. S5).

Fig. 6 a shows the effect of increasing oxamate concentrations when pyruvate was used as the variable substrate. Oxamate induced a concentration-dependent increase in the slope of the Hanes–Woolf plots when pyruvate was varied, with a simultaneous increase in the modulus of the x-intercept, yielding parallel lines. This behavior is consistent with an apparent competitive inhibition mechanism with respect to pyruvate under the tested conditions, suggesting that oxamate competes with the

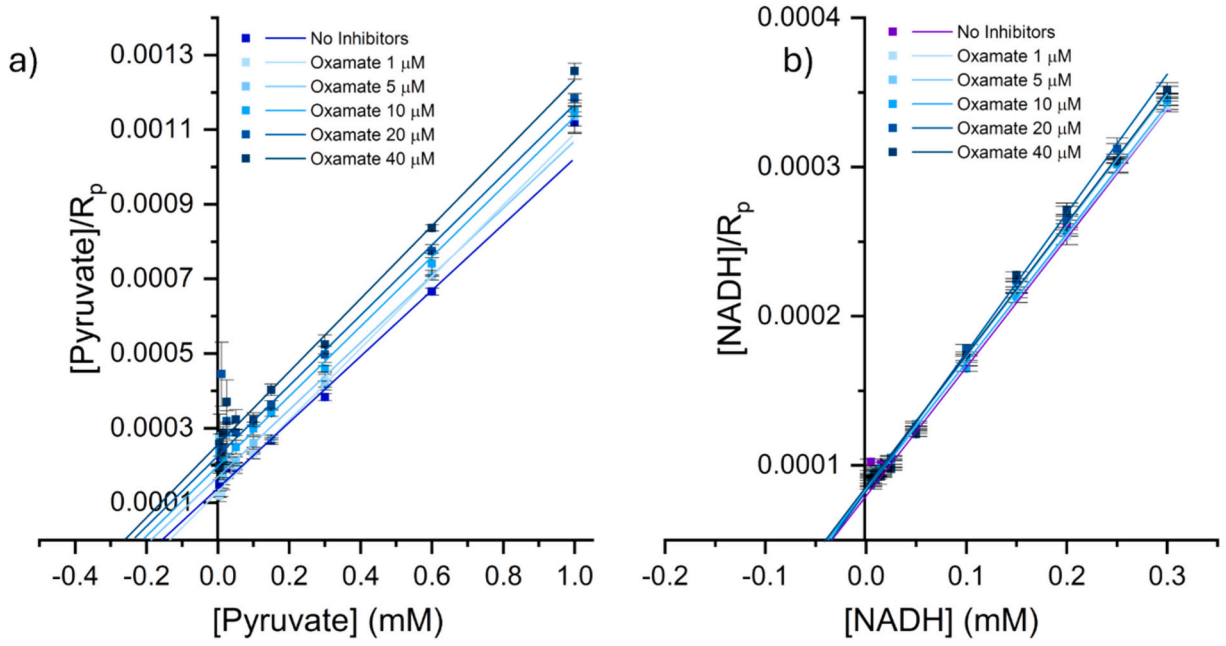

Fig. 6. Hanes–Woolf plots for the forward hLDH-A reaction in the presence of increasing concentrations of oxamate. (a) Linearization obtained by varying pyruvate concentration in the presence of 0.23 mM NADH. (b) Linearization obtained by varying NADH concentration with pyruvate equal to 1.63 mM. Data points represent mean values ± standard deviation from triplicate measurements, while solid lines correspond to linear fits.

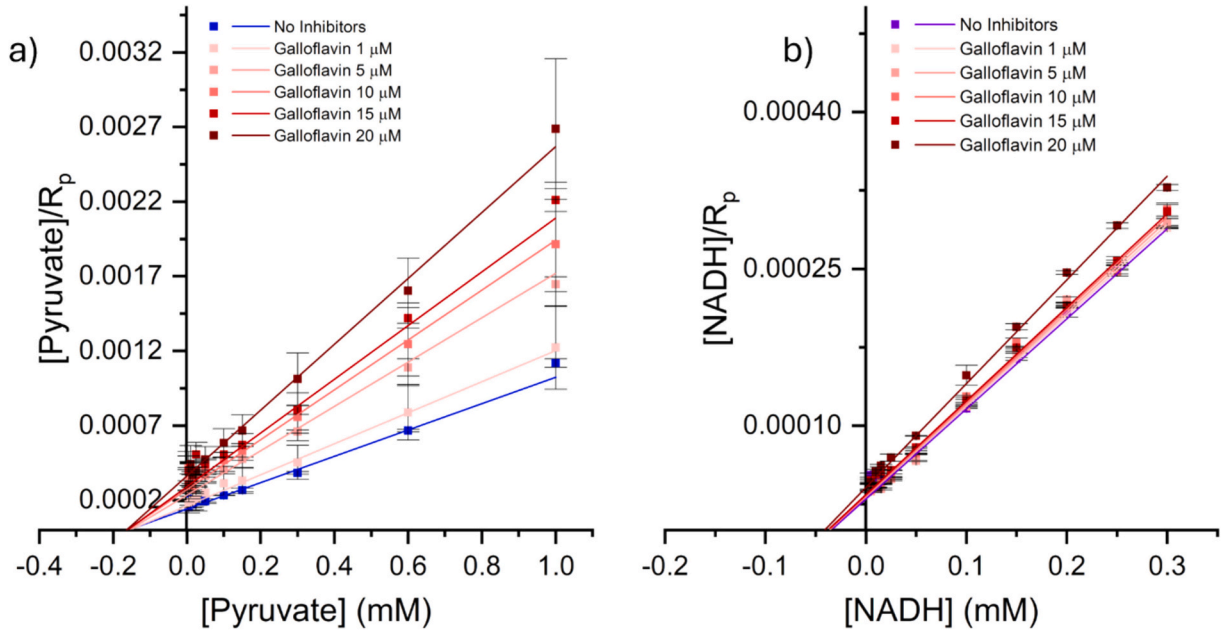

Fig. 7. Hanes–Woolf plots for the forward hLDH-A reaction in the presence of increasing concentrations of galloflavin. (a) Linearization obtained by varying pyruvate concentration in the presence of 0.23 mM NADH. (b) Linearization obtained by varying NADH concentration with pyruvate equal to 1.63 mM. Data points represent mean values ± standard deviation from triplicate measurements, while solid lines correspond to linear fits.

substrate for binding at the active site [82–85]. The corresponding Michaelis–Menten curves (Fig. S4 a) showed a progressive rightward shift with increasing oxamate concentration, accompanied by preservation of the apparent maximum reaction rate, further supporting a competitive inhibition model. By contrast, when NADH was the varied substrate, oxamate did not introduce systematic changes in Hanes-Woolf representation (Fig. 6 b, Fig. S5 a), supporting the interpretation that its primary inhibitory effect is associated with pyruvate-dependent kinetics rather than cofactor-dependent steps.

By contrast, increasing galloflavin concentrations resulted in progressively steeper Hanes-Woolf slopes (Fig. 7 a), accompanied by changes in y-intercept, but not in x-intercepts, when pyruvate concentrations were varied. This behavior is consistent with a non-competitive inhibition mechanism with respect to pyruvate (Fig. S4 b) under the tested conditions. In contrast, Hanes–Woolf plots obtained by varying NADH concentration at fixed pyruvate (Fig. 7 b) showed approximately superimposable curves. However, at a galloflavin concentration of 20 μM, the data suggest a deviation consistent with non-competitive behavior [86–89]. This observation indicates that galloflavin exerts a weaker influence on cofactor-dependent steps of the reaction compared

to substrate-dependent steps.

To further support the selected inhibition patterns, ANOVA-based comparisons of the Hanes–Woolf regressions were performed for diagnostically relevant cases. In particular, NADH-dependent profiles in the presence of oxamate were analyzed to assess whether the inhibitor produced systematic cofactor-dependent changes, whereas pyruvate-dependent profiles in the presence of galloflavin were evaluated to support the non-competitive pattern inferred from changes in slope and intercept. These analyses provided statistical support for the observed trends, although they were used as complementary evidence rather than as a substitute for global inhibition model fitting. In particular, the NADH-dependent kinetic profiles obtained in the presence of oxamate were analyzed to verify the absence of significant changes in the regression parameters, supporting the conclusion that oxamate does not appreciably affect cofactor-dependent kinetics. However, statistically significant differences were detected at some NADH concentrations. These differences did not follow a coherent inhibitor concentration-dependent trend in the Hanes–Woolf representation and were not associated with systematic changes in slope or intercept compatible with a defined inhibition pattern with respect to NADH. Therefore, these results were not interpreted as evidence of an NADH-dependent inhibition mechanism. Rather, when considered together with the pyruvate-variable assays, they support the interpretation that the primary inhibitory effect of oxamate is associated with pyruvate-dependent kinetics.

Conversely, the pyruvate-dependent Hanes–Woolf regressions obtained in the presence of galloflavin showed statistically significant changes in the regression slope, but not in the x-intercept, which is consistent with the non-competitive inhibition pattern inferred from the kinetic analysis. These analyses provided statistical support for the observed trends, although they were used as complementary evidence rather than as a substitute for global inhibition model fitting.

The corresponding F and p values are reported in the Supporting Information (Table S3).

In addition to oxamate and galloflavin, the inhibitory effects of NHI-2, FX11, and gossypol were investigated using the same kinetic approach. The complete set of linearized plots and corresponding Michaelis–Menten kinetic curves is reported in the Supporting Information (Figs. S4–S6).

NHI-2 induced marked alterations in the kinetic behavior of *h*LDH-A. When pyruvate was the variable substrate, Hanes–Woolf plots (Fig. S6 a) showed concentration-dependent changes in both slope and intercept, suggesting a mixed inhibition mechanism with respect to pyruvate. This behavior could indicate that NHI-2 may interfere not only with substrate binding but also with catalytic turnover. Consistently, the corresponding Michaelis–Menten curves displayed both a reduction in the apparent maximum reaction rate and a shift toward higher substrate concentrations at increasing inhibitor levels (Fig. S4 c). When NADH was the variable substrate, NHI-2 did not induce appreciable changes in the kinetic behavior at concentrations below 10 μM. In this concentration range, the kinetic curves (Fig. S5 c) remained essentially superimposable with the control condition, indicating a negligible influence of the inhibitor on cofactor-dependent steps.

Above this threshold concentration, NHI-2 produced significant alterations in both slope and intercept of the Hanes–Woolf plots (Fig. S6 b), consistent with the onset of a mixed inhibition mechanism involving NADH. This concentration-dependent behavior suggests that, at low inhibitor levels, NHI-2 preferentially affects substrate-related steps of the catalytic cycle, while higher inhibitor concentrations are required to significantly perturb cofactor binding and turnover [90]. Such threshold effects are commonly observed for inhibitors displaying differential affinity toward distinct enzyme states or binding modes and are particularly relevant for NAD-dependent dehydrogenases, where the cofactor often binds with high intrinsic affinity [80,91,92]. The emergence of mixed inhibition only above a critical inhibitor concentration, therefore, reflects the hierarchical sensitivity of substrate- and cofactor-dependent steps within the *h*LDH-A catalytic mechanism.

Gossypol showed the strongest inhibitory effect among the tested compounds. Hanes–Woolf plots obtained by varying pyruvate concentration (Fig. S6 c) displayed substantial increases in slope with increasing inhibitor concentration, while the x-intercept remained essentially unchanged. This behavior suggests a predominant non-competitive inhibition mechanism with respect to pyruvate under the tested conditions, indicating that gossypol primarily affects catalytic turnover rather than substrate binding. Similar differential effects have been reported in kinetic studies of LDH, where gossypol exhibited non-competitive behavior toward pyruvate [93,94].

When NADH was varied (Fig. S6 d), gossypol exhibited a more complex and concentration-dependent behavior. At inhibitor concentrations below 10 μM, the Hanes-Woolf plots appeared approximately parallel, suggesting a competitive-like behavior with respect to the cofactor [95–97]. Above this threshold, however, the linearized curves became progressively less ordered, with increasing slopes and non-systematic intercepts, indicative of a mixed-type inhibition mechanism. This transition suggests that, at low inhibitor concentrations, gossypol may primarily affect cofactor-related kinetic steps, giving rise to an apparent competitive-like inhibition. At higher concentrations, additional effects on other steps of the catalytic cycle may become relevant. Such concentration-dependent shifts in apparent inhibition modality are consistent with inhibitors that bind with different affinities to distinct enzyme states, including the free enzyme, substrate-bound complexes, and cofactor-bound forms. This behavior has been widely reported for broad-spectrum inhibitors of NAD-dependent dehydrogenases and reflects the complex coupling between substrate binding, cofactor association, and catalytic turnover [9,56,98].

The corresponding Michaelis–Menten curves (Fig. S4 d, Fig. S5 d) showed a pronounced reduction in apparent maximum reaction rate mainly at higher concentrations, consistent with strong inhibition of *h*LDH-A catalytic activity. These findings align with the well-documented broad inhibitory profile of gossypol toward dehydrogenases and other NAD-dependent enzymes.

FX11 exhibited a distinct inhibition pattern. Hanes–Woolf plot (Fig. S6 e), obtained by varying pyruvate concentration, revealed a progressive increase in slope. In contrast, no change in x-intercept was visible, suggesting a non-competitive inhibition mechanism with respect to pyruvate. When NADH was the variable substrate, the corresponding Hanes–Woolf plots showed a pronounced effect on the x-intercept with comparable changes in slope (Fig. S6 f), suggesting that FX11 exerts a mixed-type behavior, affecting both the catalytic turnover and the cofactor binding. The Michaelis–Menten curves (Fig. S4 e, Fig. S5 e) confirmed a strong concentration-dependent decrease in apparent maximum velocity under both experimental conditions. This behavior is consistent with the reported mechanism of FX11 as a potent LDH inhibitor that disrupts enzyme activity through both active-site and allosteric interactions.

Overall, the kinetic effects induced by the investigated inhibitors, including variations in the apparent maximum reaction rate and Michaelis constant and the corresponding inhibition mechanisms inferred from Hanes–Woolf analysis, are summarized in Table 2 and Table 3, regarding Pyruvate and NADH variations, respectively, providing a comparative overview of their impact on *h*LDH-A catalytic

Table 2
Summary of the inhibitory effect of the tested compounds when pyruvate was the variable substrate. The direction of the arrow indicates the change in the parameter with respect to the uninhibited condition.

Inhibitor	Effect on $R_{p,max}$	Effect on K_M	Predominant apparent inhibition mechanism
Oxamate	≈	▲	Competitive
Galloflavin	▼	≈	Non-competitive
NHI-2	▼	▼	Mixed-type
Gossypol	▼	≈	Non-competitive
FX11	▼	≈	Non-competitive

Table 3
Summary of the inhibitory effect of the tested compounds when NADH was the variable substrate. The direction of the arrow indicates the change in the parameters with respect to the uninhibited condition.

Inhibitor	Effect on $R_{p,max}$	Effect on K_M	Predominant apparent inhibition mechanism
Oxamate	≈	≈	No effect
Galloflavin	≈	≈	No effect below 20 μM
	▼	≈	Non-competitive at 20 μM
NHI-2	≈	≈	No effect below 10 μM
	▼	▲	Mixed-type above 10 μM
Gossypol	▼	≈	Competitive below 10 μM
	▼	▲	Mixed-type above 10 μM
FX11	▼	▲	Mixed-type

behavior.

The differences in inhibitory effects underscore the importance of detailed kinetic analysis for accurately characterizing inhibitor mechanisms beyond simple activity measurements.

To rationalize the inhibition mechanisms identified through kinetic analysis, three-dimensional representations of the investigated compounds were generated, together with the three-dimensional representation of *h*LDH-A, as shown in Fig. 8.

The apparent competitive inhibition exhibited by oxamate is consistent with its structural similarity to pyruvate, supporting direct competition at the substrate-binding site. In contrast, the larger and more structurally complex architectures of galloflavin, gossypol, and FX11 may support interaction modes involving regions beyond the substrate-binding pocket. This interpretation is consistent with their predominantly non-competitive inhibition patterns in the tested conditions. NHI-2, displaying intermediate molecular features, may interact with multiple enzyme states, consistent with its mixed-type inhibition profile.

To provide orthogonal structural support to the inhibition mechanisms inferred from kinetic analysis, molecular docking analyses were performed for the investigated inhibitors [34–36]. Representative docking poses are reported in Fig. S7, while the main ligand–protein interactions, including hydrogen bonds with specific amino acid residues, are summarized in Table S4.

Docking analysis allowed identification of the predicted binding region occupied by each ligand and of the main interactions established within the enzymatic pocket. Oxamate was predicted to bind within the substrate-binding region, forming interactions with residues involved in substrate recognition. This result is consistent with its competitive inhibition toward pyruvate, as inferred from the kinetic analysis. In contrast, galloflavin, NHI-2, and FX11 showed binding poses involving residues located outside or adjacent to the substrate-binding region. These interaction patterns are compatible with non-competitive or mixed-type inhibition, since they suggest that these compounds do not simply compete with pyruvate for the substrate-binding site but may interfere with catalytic turnover and/or cofactor-associated enzyme states.

In the case of gossypol, docking suggested a possible interaction with the NADH-associated region, which is compatible with the competitive-like behavior observed at low inhibitor concentrations when NADH was varied. However, the kinetic analysis revealed a more complex concentration-dependent behavior, including non-competitive

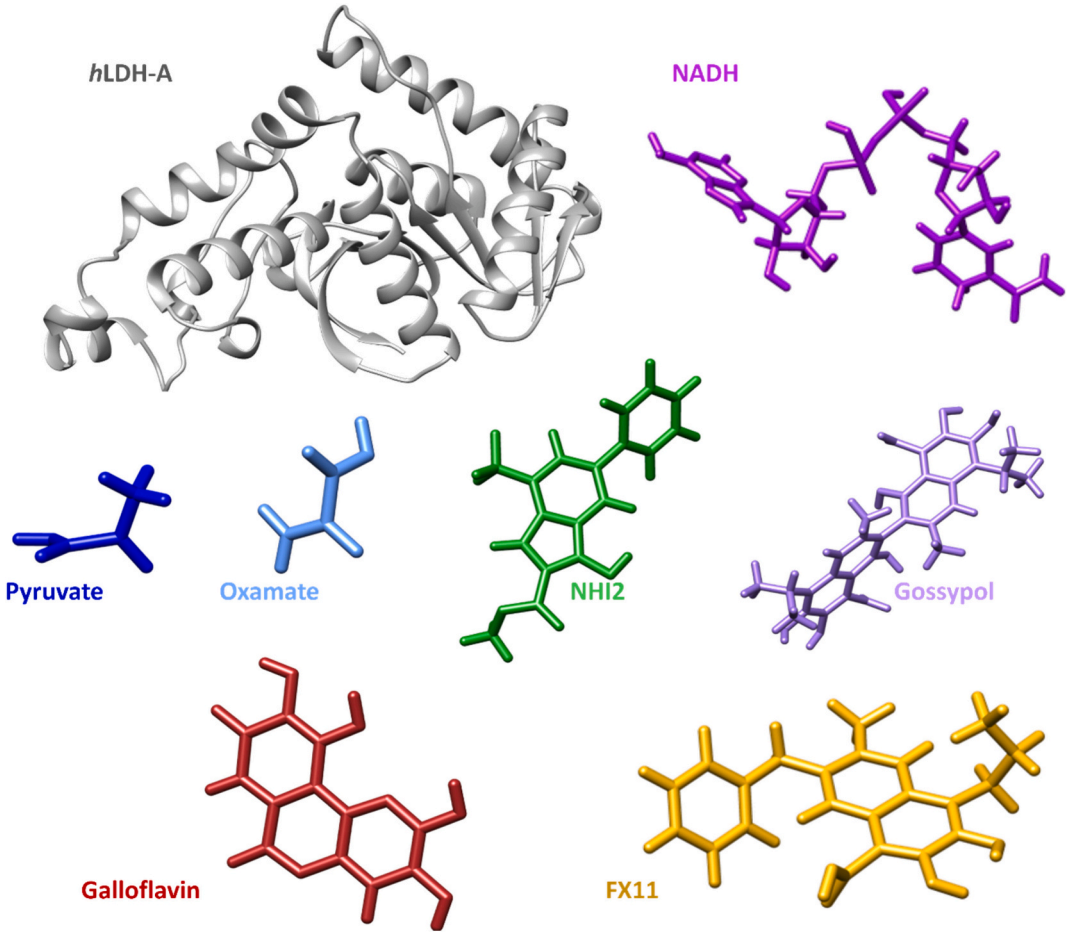

Fig. 8. Structural overview of hLDH-A and investigated ligands. Molecules are shown at comparable scale to highlight differences in size, structural complexity, and aromatic character. Structures were rendered using UCSF Chimera for qualitative visualization purposes.

inhibition with respect to pyruvate and mixed-type features at higher gossypol concentrations. Therefore, gossypol was not interpreted as a purely competitive inhibitor, but rather as a compound potentially able to interact with multiple enzyme states or regions within the catalytic/cofactor-binding environment.

Overall, docking provided qualitative structural support for distinguishing the competitive behavior of oxamate from the non-competitive or mixed-type profiles of the other inhibitors by highlighting ligand localization and hydrogen-bond interactions with specific residues. Nevertheless, the inhibition mechanisms were not assigned on the basis of docking alone.

Beyond qualitative classification of inhibition patterns, inhibitor potency was quantitatively assessed by determining inhibition constants for the forward reaction under pyruvate-variation conditions, as described in Section 2.2.5. The corresponding secondary plots used for K_i extraction are reported in the Supporting Information (Fig. S8), while the calculated values are summarized in Table 4. In all cases, the secondary plots showed linear trends compatible with the apparent inhibition patterns inferred from Hanes-Woolf analysis. The inhibition constants were calculated from the x-intercepts of the respective linear regressions.

To assess the robustness of K_i determination, the regressions underlying inhibitor-constant extraction were statistically evaluated. As reported in the Supporting Information (Table S5), the secondary plots used for K_i calculation showed acceptable linearity, supporting the consistency of the inhibition models used for K_i estimation. The associated confidence intervals confirmed that the uncertainty of K_i determination did not affect the relative potency ranking of the investigated inhibitors.

The determined K_i values fall within the micromolar range for all investigated compounds, revealing a clear hierarchy of inhibitory potency toward *h*LDH-A under forward reaction conditions. Among the tested inhibitors, gossypol and galloflavin exhibited the lowest K_i values, indicating the strongest affinity for the enzyme in the adopted experimental setup. These values are consistent with previously reported data describing both compounds as effective LDH-A inhibitors with low micromolar potency. Manerba et al. reported that galloflavin displays K_i value of 5.64 μM against *h*LDH-A when evaluated under substrate-variation conditions [89]. Although the value obtained here is approximately two-fold higher, the differences are reasonably attributable to variations in buffer composition, enzyme preparation, temperature, substrate concentration regime, and kinetic modeling assumptions.

Gossypol has been previously described to exhibit an inhibition constant of approximately 20 μM [94] against LDH-A, when evaluated under pyruvate-variable conditions. The value reported here is lower, but therefore in agreement with literature values. However, most recent studies have reported substantially lower values of the inhibition constant, but they are often determined under NADH-variation conditions or at specific cofactor concentrations. Since gossypol has been shown to interact with multiple enzyme states, including cofactor-bound forms, its apparent inhibitory strength is strongly influenced by the NADH concentration used during kinetic evaluation. Consequently, direct numerical comparison requires careful consideration of the experimental configuration adopted in each study.

FX11 displayed a K_i of 25.2 μM. In the seminal study by Le et al., FX11 was characterized as an LDH-A inhibitor with a reported K_i of approximately 8 μM, determined under NADH-variation conditions [99]. The higher K_i observed in the present work is consistent with the different kinetic configuration adopted here, as FX11 has been described to preferentially interfere with cofactor-dependent steps. Therefore, K_i values determined under pyruvate-variation conditions are not expected to be directly superimposable with those obtained when NADH is the variable ligand.

Oxamate exhibited a Ki of 52.5 μM. Fiume et al. reported a Ki of 99 μM for oxamate against human LDH-A, while other biochemical studies have described values in the several tens of micromolar range depending on assay conditions [88,100]. The present value is therefore consistent with its established role as a moderate competitive analog of pyruvate.

NHI-2 showed a Ki of 49.1 μM. In the literature, NHI-2 and related N-hydroxyindole derivatives are often reported with IC50 values in the low micromolar range rather than directly measured Ki values [90]. Because IC50 values depend on substrate concentration and assay configuration, a direct numerical comparison is not straightforward. Nevertheless, the micromolar potency observed here remains compatible with previously described inhibitory activity for this compound class.

To provide a more structured comparison with literature data, the main quantitative and methodological considerations are summarized in Table 5.

Overall, the quantitative ranking of inhibitory potency observed in this study is coherent with previously reported biochemical trends, and minor numerical differences can be rationalized by differences in kinetic regime, ligand variation strategy, and experimental conditions.

3.5. Model validation and predictive capability

The proposed kinetic model was evaluated by comparing simulated NADH concentration profiles and experimental data obtained under fixed initial conditions. As shown in Fig. 9a and b, the experimental NADH concentrations, determined using the calibration curve reported in Fig. S9, exhibit a non-negligible degree of dispersion, which becomes more pronounced at longer reaction times. This behavior can be rationalized considering the very low enzyme concentration employed in the validation experiments, which was deliberately selected to slow down the reaction kinetics, avoid enzyme aggregation, and enable time-resolved monitoring. Under these conditions, the absolute variations in NADH concentration over time are inherently small, and, as a consequence, the signal-to-noise ratio is reduced. A preliminary comparison based on a simplified kinetic model, considering only the forward reaction, revealed poor agreement with the experimental data, as

Table 4
Inhibition constants for the different tested compounds.

Inhibitor	K_i (μM)
Oxamate	52.5 ± 2
Galloflavin	15.0 ± 0.2
NHI-2	49.1 ± 3
Gossypol	6.9 ± 0.1
FX11	25.2 ± 0.9

Table 5
Structured comparison of inhibitor potency with literature benchmarks.

Inhibitor	Determined K_i [μM]	Relative potency	Literature benchmark	Interpretation
Oxamate	52.5 ± 2.0	Moderate	K_i = 99 μM against hLDH-A [88,100]	Consistent reference inhibitor
Galloflavin	15.0 ± 0.2	High	K_i = 5.64 μM against hLDH-A [89]	Comparable potency range
NHI-2	49.1 ± 3.0	Moderate	Low-micromolar IC50 values reported [90]	K_i and IC50 not directly comparable
Gossypol	6.9 ± 0.1	Highest	K_i ≈ 20 μM under pyruvate-variable conditions [94]	Strong inhibition, assay-dependent
FX11	25.2 ± 0.9	Intermediate	K_i ≈ 8 μM under NADH-variable conditions [99]	Mechanism-dependent comparison

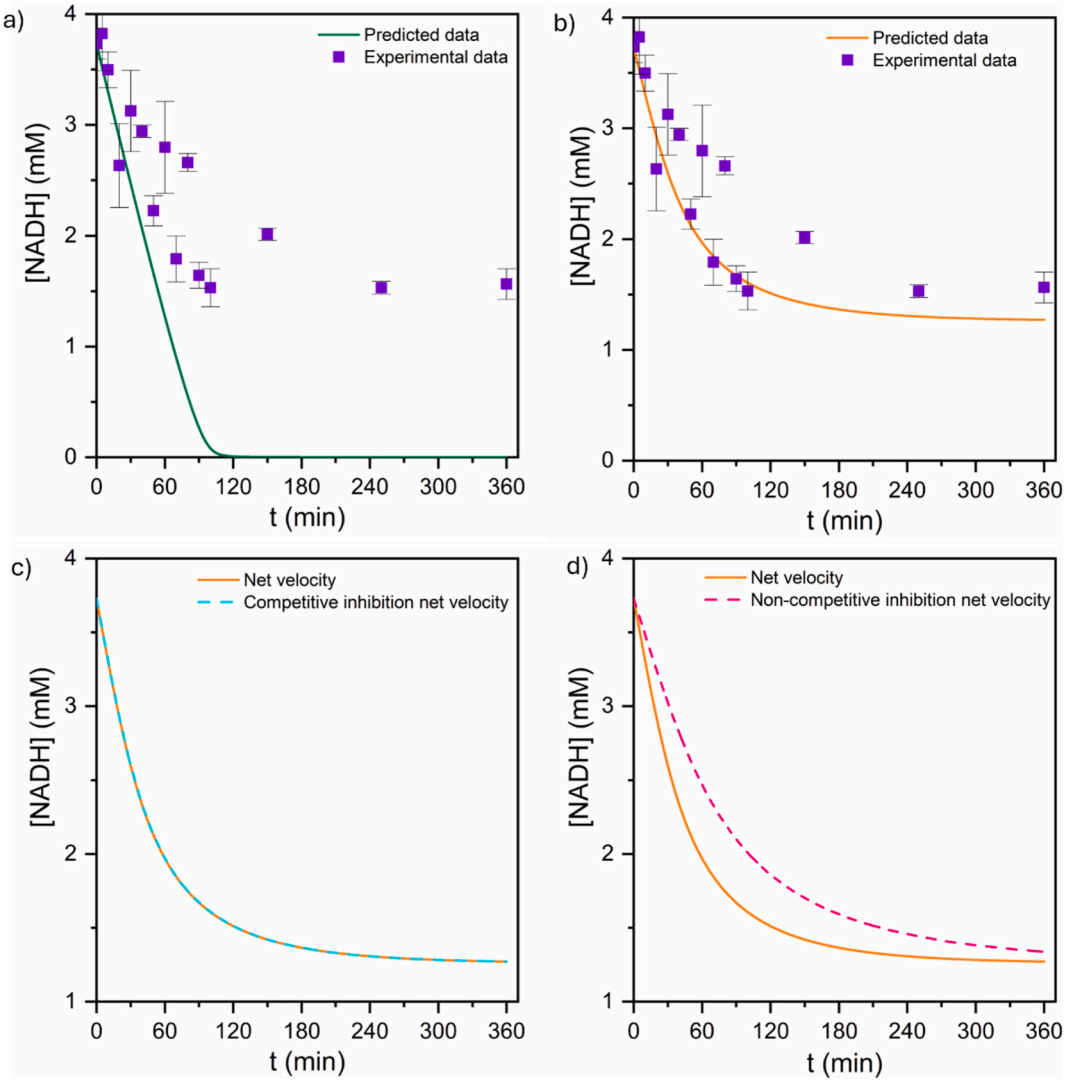

Fig. 9. Experimental validation of the kinetic model and simulation of inhibition effects. (a) Forward-reaction-only model compared with experimental data; (b) net-rate model compared with experimental data; (c) simulated competitive inhibition (oxamate) and (d) simulated non-competitive inhibition (FX11), compared with uninhibited net-rate model. Symbols represent experimental data, while lines represent model predictions.

shown in Fig. 9 a, particularly at intermediate and long reaction times. This result highlights the inadequacy of neglecting reaction reversibility in the kinetic description of LDH.

In contrast, implementation of the full mechanistic model, based on the net reaction rate defined as the difference between forward and reverse contributions, led to a markedly improved agreement with the experimental observations, as evident from Fig. 9 b. The model captures both the initial rapid decrease in NADH concentration and the subsequent approach to a steady-state regime, demonstrating that explicit consideration of reversibility is essential to correctly describe the kinetic behavior of the system. Notably, this level of agreement was achieved without the inclusion of additional kinetic terms, indicating that the dominant features of the system can be adequately captured within a minimal mechanistic framework. The agreement between simulation and experiment was positive ($R^2 = 0.688$; Er $\leq$ 14%). Nevertheless, the model considers the dominant NADH consumption trend and provides a clear improvement over the forward-only kinetic description, supporting the importance of explicitly accounting for reaction reversibility. The R^2 value was therefore interpreted together with the relative error (Er $\leq$ 14%), the dispersion of the validation data, and the intentionally minimal formulation of the model. In nonlinear biochemical and enzymatic modeling, moderate coefficients of determination may also be expected, due to experimental variability and complex reaction mechanisms [101,102].

The moderate agreement between model and experiment may also reflect processes not explicitly represented in the minimal framework, including dynamic conformational transitions. However, explicit conformational modeling would require independent kinetic or structural parameters not available in the present study.

These values indicate that the model captures the main qualitative trend of NADH consumption under the tested conditions, although they do not support its interpretation as a broadly predictive simulator. Therefore, the model should be regarded as a qualitative-to-semi-quantitative mechanistic framework, useful for interpreting the dominant kinetic behavior of the system rather than for accurately predicting NADH concentration profiles under all possible experimental conditions.

Although the model captures the main trends of NADH consumption, a systematic deviation from experimental data is observed at longer reaction times, where the measured NADH concentration approaches a higher plateau value than predicted. This discrepancy suggests that additional processes not explicitly included in the minimal model may contribute to the late-stage reaction behavior. In fact, as the system approaches equilibrium, the net reaction rate becomes very small, and

the concentration profile becomes increasingly sensitive to minor experimental uncertainties [11]. Under these conditions, even small absolute deviations in absorbance measurements may translate into noticeable differences in the estimated NADH concentration. In addition, the simplified kinetic model assumes ideal behavior and constant catalytic activity, whereas in real systems, slight deviations from these assumptions, such as minor enzyme deactivation over time or subtle shifts in the effective equilibrium position, may contribute to a residual NADH concentration higher than that predicted by the model [11,103].

The model was intentionally formulated as a minimal mechanistic description, focusing on the ordered sequential bi–bi mechanism without including additional effects such as substrate inhibition. However, an extended version of the kinetic model including substrate and product inhibition terms was also evaluated. The corresponding dissociation constants were taken from literature data and incorporated into the denominator of the reversible ordered bi–bi rate equation [104,105]. The comparison between the extended model and the minimal model is reported in the Supporting Information (Fig. S10).

The inclusion of substrate and product inhibition did not appreciably modify the agreement between simulated and experimental NADH concentration profiles under the validation conditions adopted in this work. The temporal evolution of NADH was already adequately described by the reversible ordered bi–bi model, indicating that reaction reversibility was the dominant kinetic contribution required to reproduce the observed progress curves. Moreover, the additional inhibition constants were not experimentally determined under the present assay conditions, and their introduction increased the number of assumptions and the computational complexity of the model without producing a measurable improvement in predictive capability.

For these reasons, substrate and product inhibition were acknowledged as experimentally observable phenomena but were not included in the final kinetic model used in the main analysis. The model was intentionally maintained as a minimal mechanistic framework able to integrate forward and reverse catalysis, thermal deactivation, and inhibitor-dependent effects while preserving parameter identifiability and interpretability.

Following model validation, the kinetic framework was further employed to simulate the effect of enzyme inhibition. Competitive and non-competitive inhibition scenarios were implemented by incorporating the corresponding inhibition terms into the kinetic equations. Competitive inhibition was modeled using the inhibition constant experimentally determined for oxamate, while non-competitive inhibition was described using the K_i value obtained for FX11.

The simulations reveal distinct effects depending on the inhibition mechanism. In the case of competitive inhibition (Fig. 9 c), the presence of the inhibitor leads to negligible or absent differences compared to the uninhibited system. This behavior can be rationalized considering the relatively high pyruvate concentration adopted in the simulations, which effectively reduces the impact of the competitive inhibitor. Under these conditions, substrate binding is favored, and the inhibitor, present at a concentration of 20 μM, does not significantly alter the overall reaction kinetics.

In contrast, non-competitive inhibition (Fig. 9 d) produces a more pronounced effect on the reaction dynamics, resulting in slower NADH consumption and a higher residual concentration at longer reaction times. This behavior reflects a reduction in the effective catalytic activity of the enzyme, as non-competitive inhibitors affect both the free enzyme and enzyme–substrate complexes, independently of the substrate concentration.

The inhibitor simulations should also be interpreted qualitatively. Their purpose was to compare the expected kinetic signatures associated with competitive and non-competitive inhibition within the same reversible mechanistic framework, rather than to provide fully quantitative predictions of inhibitor-dependent reaction time courses.

Overall, the model captures the expected qualitative differences between inhibition mechanisms and highlights the strong dependence of competitive inhibition on substrate concentration, in contrast with the more robust effect observed for non-competitive inhibitors.

4. Conclusions

In this study, the kinetic behavior of human lactate dehydrogenase A (*h*LDH-A) was systematically investigated through a comprehensive and mechanistic approach. Steady-state kinetic parameters were determined for both the forward and reverse reaction under physiological-like conditions, allowing the identification of intrinsic kinetic constants within the framework of an ordered sequential bi–bi catalytic mechanism.

The kinetic analysis revealed a pronounced asymmetry between the two reaction directions, with the pyruvate-to-lactate conversion displaying a markedly higher catalytic throughput compared to the reverse reaction. Despite a stronger apparent affinity toward lactate, the reverse reaction proceeds with significantly lower reaction rates, highlighting that substrate binding alone does not dictate catalytic efficiency. Instead, cofactor-dependent steps and associated conformational transitions emerge as key determinants of enzymatic flux, in agreement with the central physiological role of *h*LDH-A in sustaining NAD^+ regeneration and glycolytic metabolism.

Establishing such a detailed kinetic reference is a prerequisite for any meaningful evaluation of enzyme inhibition. In the absence of a solid kinetic framework, apparent reductions in enzymatic activity may arise from variations in substrate or cofactor availability, changes in kinetic regime, or experimental artefacts, rather than from genuine inhibitory effects. This limitation is particularly critical for bi-substrate enzymes such as lactate dehydrogenase, whose activity reflects a complex coupling between substrate binding, cofactor association, and catalytic turnover.

Building on this kinetic framework, the inhibitory effects of a panel of reference LDH inhibitors were analyzed in detail. The combined evaluation of Michaelis–Menten curves and Hanes–Woolf linearization, supported by a nonlinear fitting of raw data, enabled identification of predominant inhibition patterns under defined assay conditions, revealing distinct modes of enzyme perturbation. While oxamate behaved as a classical competitive inhibitor with respect to pyruvate, galloflavin, FX11, and gossypol predominantly affected catalytic turnover without significantly altering substrate affinity. In contrast, NHI-2 exhibited mixed and concentration-dependent inhibition patterns, indicative of interference with multiple steps of the catalytic cycle.

The identified inhibition mechanisms were further qualitatively supported by molecular docking simulations.

Among the tested compounds, gossypol displayed the strongest inhibitory effect and the most complex kinetic behavior. Its non-competitive inhibition with respect to pyruvate, combined with a competitive-like interaction toward NADH at low concentrations and a transition to mixed inhibition at higher levels, supports a model in which gossypol binds with different affinities to multiple enzyme states. This concentration-dependent shift in apparent inhibition modality reflects the intrinsic coupling between substrate binding, cofactor association, and catalytic turnover characteristic of NAD-dependent dehydrogenases. Ki values were determined under pyruvate-variable assay conditions and, therefore, they should be interpreted as standardized, condition-specific inhibition constants.

Based on the experimentally determined kinetic parameters, a mechanistic model describing the net reaction rate was derived and validated through comparison with experimental progress curves. The results demonstrate that explicit consideration of reaction reversibility is required to capture the main trend of the observed temporal evolution of NADH concentration, whereas simplified models considering only the forward reaction fail to reproduce the experimental behavior. Moreover, the inclusion of additional substrate or product inhibition terms did not improve the agreement between experimental data and model predictions under the validation conditions. Therefore, the model was

intentionally retained as a minimal reversible framework, providing an interpretable description of the dominant kinetic behavior by balancing mechanistic interpretability with model simplicity.

Although minor deviations between simulations and experimental measurements were observed at longer reaction times, the model describes the dominant kinetic features of the system while maintaining a minimal mechanistic formulation. Furthermore, the model was able to qualitatively reproduce the different kinetic effects associated with competitive and non-competitive inhibition mechanisms.

Overall, this work establishes a robust kinetic framework for the evaluation of *h*LDH-A catalysis and its modulation. The known LDH inhibitors investigated in this study were used as benchmark compounds to compare different inhibition mechanisms under standardized experimental conditions. The main contribution of the work therefore lies in the establishment of an experimentally grounded kinetic reference for *h*LDH-A, integrating forward and reverse catalysis, substrate and cofactor dependence, intrinsic kinetic parameters, inhibitor-dependent kinetic profiles, and reaction reversibility within a single framework. This integrated approach provides a useful basis for distinguishing genuine inhibitory effects from assay-dependent or kinetic artefacts. In addition, the mechanistic model developed in this study reproduces the main features of the experimental progress curves and highlights the importance of explicitly accounting for reaction reversibility in the kinetic description of LDH. Together, these results enable discrimination between genuine inhibitory effects and indirect or artefactual changes in enzymatic activity, thereby supporting the development of enzyme-based analytical platforms for the screening of potential anticancer drugs. The kinetic parameters and mechanistic insights reported here may also facilitate the rational design and optimization of LDH-based biosensing systems for analytical and biomedical applications.

CRediT authorship contribution statement

Chiara Vincenzi: Writing – original draft. **Edoardo Bocina:** Investigation. **Debora Fino:** Writing – review & editing. **Carminna Ottone:** Supervision, Investigation. **Marco Piumetti:** Writing – review & editing, Supervision, Investigation.

Funding sources

No competing financial interests have been declared.

Declaration of competing interest

The authors declare that they have no known competing financial interests or personal relationships that could have appeared to influence the work reported in this paper.

Appendix A. Supplementary data

Supplementary data to this article can be found online at https://doi.org/10.1016/j.bioorg.2026.110489.

Data availability

Data will be made available on request.

References

[1] S.-K. Kim, Enzymes as targets for drug development II, Int. J. Mol. Sci. 24 (2023) 3258, https://doi.org/10.3390/ijms24043258.
[2] S. Chaturvedi, A.K. Singh, A.K. Keshari, S. Maity, S. Sarkar, S. Saha, Human metabolic enzymes deficiency: a genetic mutation based approach, Scientifica 2016 (2016) 1–14, https://doi.org/10.1155/2016/9828672.
[3] M. de la Fuente, L. Lombardero, A. Gómez-González, C. Solari, I. Angulo-Barturen, A. Acera, E. Vecino, E. Astigarraga, G. Barreda-Gómez, Enzyme therapy: current challenges and future perspectives, Int. J. Mol. Sci. 22 (2021) 9181, https://doi.org/10.3390/ijms22179181.
[4] E. Bocina, C. Cocuzza, C. Vincenzi, D. Fino, V. Cauda, M. Piumetti, Enzyme-based biosensors: emerging tools for advanced biomedical applications, Talanta 300 (2026) 129241, https://doi.org/10.1016/j.talanta.2025.129241.
[5] R. Santos, O. Ursu, A. Gaulton, A.P. Bento, R.S. Donadi, C.G. Bologa, A. Karlsson, B. Al-Lazikani, A. Hersey, T.I. Oprea, J.P. Overington, A comprehensive map of molecular drug targets, Nat. Rev. Drug Discov. 16 (2017) 19–34, https://doi.org/10.1038/nrd.2016.230.
[6] M. Schenone, V. Dančík, B.K. Wagner, P.A. Clemons, Target identification and mechanism of action in chemical biology and drug discovery, Nat. Chem. Biol. 9 (2013) 232–240, https://doi.org/10.1038/nchembio.1199.
[7] M.F. Pinto, J. Sirina, N.D. Holliday, C.L. McWhirter, High-throughput kinetics in drug discovery, SLAS Discovery 29 (2024) 100170, https://doi.org/10.1016/j.slasd.2024.100170.
[8] Y. Ma, B.E. Eser, Bridging disciplines in enzyme kinetics: understanding steady-state, transient-state and performance parameters, Catalysts 15 (2025) 1139, https://doi.org/10.3390/catal15121139.
[9] R.A. Copeland, Evolution of the drug-target residence time model, Expert Opin. Drug Discov. 16 (2021) 1441–1451, https://doi.org/10.1080/17460441.2021.1948997.
[10] J. Dong, On catalytic kinetics of enzymes, Processes 9 (2021) 271, https://doi.org/10.3390/pr9020271.
[11] Athel. Cornish-Bowden, Fundamentals of Enzyme Kinetics, Wiley, 2013.
[12] U. Aday, A. Böyük, H. Akkoç, The prognostic significance of serum lactate dehydrogenase-to-albumin ratio in colorectal cancer, Ann. Surg. Treat. Res. 99 (2020) 161, https://doi.org/10.4174/astr.2020.99.3.161.
[13] F. Cascardo, N. Anselmino, A. Páez, E. Labanca, P. Sanchis, V. Antico-Arciuch, N. Navone, G. Gueron, E. Vázquez, J. Cotignola, HO-1 modulates aerobic glycolysis through LDH in prostate cancer cells, Antioxidants 10 (2021) 966, https://doi.org/10.3390/antiox10060966.
[14] B. Cui, Y. Luo, P. Tian, F. Peng, J. Lu, Y. Yang, Q. Su, B. Liu, J. Yu, X. Luo, L. Yin, W. Cheng, F. An, B. He, D. Liang, S. Wu, P. Chu, L. Song, X. Liu, H. Luo, J. Xu, Y. Pan, Y. Wang, D. Li, P. Huang, Q. Yang, L. Zhang, B.P. Zhou, S. Liu, G. Xu, E. W.-F. Lam, K.W. Kelley, Q. Liu, Stress-induced epinephrine enhances lactate dehydrogenase a and promotes breast cancer stem-like cells, J. Clin. Invest. 129 (2019) 1030–1046, https://doi.org/10.1172/JCI121685.
[15] Y. Wei, H. Xu, J. Dai, J. Peng, W. Wang, L. Xia, F. Zhou, Prognostic significance of serum lactic acid, lactate dehydrogenase, and albumin levels in patients with metastatic colorectal cancer, Biomed. Res. Int. 2018 (2018) 1–8, https://doi.org/10.1155/2018/1804086.
[16] C. Cocuzza, C. Vincenzi, C. Ottone, A. Illanes, D. Fino, V. Cauda, M. Piumetti, Synthesis and characterization of mesoporous silicas with dendritic and spongy-like structures: potential supports for human lactate dehydrogenase-based microreactors aimed at anticancer inhibitor screening, Microporous Mesoporous Mater. 376 (2024) 113182, https://doi.org/10.1016/j.micromeso.2024.113182.
[17] C. Vincenzi, C. Cocuzza, A. Illanes, D. Fino, S. Hernández, V. Cauda, C. Ottone, M. Piumetti, Comparative analysis of electrochemical and spectroscopic sensing of enzymatic reactions: lactate dehydrogenase-a case study, Microchem. J. 219 (2025) 115963, https://doi.org/10.1016/j.microc.2025.115963.
[18] K. Augoff, A. Hryniewicz-Jankowska, R. Tabola, Lactate dehydrogenase 5: an old friend and a new hope in the war on cancer, Cancer Lett. 358 (2015) 1–7, https://doi.org/10.1016/j.canlet.2014.12.035.
[19] International Agency for Research on Cancer. https://gco.iarc.who.int/tomorrow/en/dataviz/trends?multiple_populations=1, 2022 accessed January 19, 2026.
[20] P. Tang, J. Xu, C.L. Oliveira, Z.J. Li, S. Liu, A mechanistic kinetic description of lactate dehydrogenase elucidating cancer diagnosis and inhibitor evaluation, J. Enzyme Inhib. Med. Chem. 32 (2017) 564–571, https://doi.org/10.1080/14756366.2016.1275606.
[21] S. Shibata, S. Sogabe, M. Miwa, T. Fujimoto, N. Takakura, A. Naotsuka, S. Kitamura, T. Kawamoto, T. Soga, Identification of the first highly selective inhibitor of human lactate dehydrogenase B, Sci. Rep. 11 (2021) 21353, https://doi.org/10.1038/s41598-021-00820-7.
[22] E.-Y. Kim, T.-W. Chung, C.W. Han, S.Y. Park, K.H. Park, S.B. Jang, K.-T. Ha, A novel lactate dehydrogenase inhibitor, 1-(Phenylseleno)-4-(trifluoromethyl) benzene, suppresses tumor growth through apoptotic cell death, Sci. Rep. 9 (2019) 3969, https://doi.org/10.1038/s41598-019-40617-3.
[23] E. Varghese, S.M. Samuel, A. Líšková, M. Samec, P. Kubatka, D. Büsselberg, Targeting glucose metabolism to overcome resistance to anticancer chemotherapy in breast cancer, Cancers (Basel) 12 (2020) 2252, https://doi.org/10.3390/cancers12082252.
[24] A. Farhana, S.L. Lappin, Biochemistry, lactate dehydrogenase, 2025.
[25] J.-K. Byun, Tumor lactic acid: a potential target for cancer therapy, Arch. Pharm. Res. 46 (2023) 90–110, https://doi.org/10.1007/s12272-023-01431-8.
[26] R. Kusumawati, A.H. Nasrullah, R.N. Pesik, Muthmainah, D. Indarto, Secondary metabolites of *Mirabilis jalapa* structurally inhibit lactate dehydrogenase a in silico: a potential cancer treatment, IOP Conf. Ser.: Mater. Sci. Eng. 333 (2018) 012078, https://doi.org/10.1088/1757-899X/333/1/012078.
[27] R.J. DeBerardinis, N.S. Chandel, We need to talk about the Warburg effect, Nat. Metab. 2 (2020) 127–129, https://doi.org/10.1038/s42255-020-0172-2.
[28] M.V. Liberti, J.W. Locasale, The Warburg effect: how does it benefit cancer cells? Trends Biochem. Sci. 41 (2016) 211–218, https://doi.org/10.1016/j.tibs.2015.12.001.
[29] M.I. Koukourakis, A. Giatromanolaki, Warburg effect, lactate dehydrogenase, and radio/chemo-therapy efficacy, Int. J. Radiat. Biol. 95 (2019) 408–426, https://doi.org/10.1080/09553002.2018.1490041.

[30] P. Miao, S. Sheng, X. Sun, J. Liu, G. Huang, Lactate dehydrogenase a in cancer: a promising target for diagnosis and therapy, IUBMB Life 65 (2013) 904–910, https://doi.org/10.1002/iub.1216.

[31] Y. Feng, Y. Xiong, T. Qiao, X. Li, L. Jia, Y. Han, Lactate dehydrogenase a: a key player in carcinogenesis and potential target in cancer therapy, Cancer Med. 7 (2018) 6124–6136, https://doi.org/10.1002/cam4.1820.

[32] W. Xing, X. Li, Y. Zhou, M. Li, M. Zhu, Lactate metabolic pathway regulates tumor cell metastasis and its use as a new therapeutic target, Explor. Med. (2023) 541–559, https://doi.org/10.37349/emed.2023.00160.

[33] A. Comandatore, M. Franczak, R.T. Smolenski, L. Morelli, G.J. Peters, E. Giovannetti, Lactate dehydrogenase and its clinical significance in pancreatic and thoracic cancers, Semin. Cancer Biol. 86 (2022) 93–100, https://doi.org/10.1016/j.semcancer.2022.09.001.

[34] Y. Huang, S. Benni, U.P. Yadav, M.A. Babu, A. Verma, T.G. Singh, N. Bansal, Y. Zhang, Deploying the high-throughput virtual screening (HTVS) approach for the identification of new lactate dehydrogenase (LDH) inhibitors with anticancer assets, Sci. Rep. 16 (2026) 5921, https://doi.org/10.1038/s41598-026-36385-6.

[35] Y. Shu, J. Yue, Y. Li, Y. Yin, J. Wang, T. Li, X. He, S. Liang, G. Zhang, Z. Liu, Y. Wang, Development of human lactate dehydrogenase a inhibitors: high-throughput screening, molecular dynamics simulation and enzyme activity assay, J. Comput. Aided Mol. Des. 38 (2024) 28, https://doi.org/10.1007/s10822-024-00568-y.

[36] H. Sharma, S. Mondal, U. Urquiza, C. Esparza, S. Bartlett, L. Santa-Pinter, H. Hill, M. White, P. Sharma, L. Luckett-Chastain, A. Cooper, M. Rasel, P. Gao, K. P. Battaile, S.K. Shukla, S. Lovell, M.A. Ihnat, Synthesis and biological characterization of an orally bioavailable lactate dehydrogenase-a inhibitor against pancreatic cancer, Eur. J. Med. Chem. 275 (2024) 116598, https://doi.org/10.1016/j.ejmech.2024.116598.

[37] S. Cao, H. Li, Y. Liu, M. Zhang, M. Wang, Z. Zhou, J. Chen, S. Zhang, J. Xu, J. R. Knutson, Femtosecond fluorescence spectra of NADH in solution: ultrafast solvation dynamics, J. Phys. Chem. B 124 (2020) 771–776, https://doi.org/10.1021/acs.jpcb.9b10656.

[38] N.A. Osik, E.A. Zelentsova, K.A. Sharshov, Y.P. Tsentalovich, Nicotinamide adenine dinucleotide reduced (NADH) is a natural UV filter of certain bird lens, Sci. Rep. 12 (2022) 16850, https://doi.org/10.1038/s41598-022-21139-x.

[39] F.C. Onyeogaziri, C. Papaneophytou, A general guide for the optimization of enzyme assay conditions using the design of experiments approach, SLAS Discovery 24 (2019) 587–596, https://doi.org/10.1177/2472555219830084.

[40] C. Cocuzza, E. Antoniono, C. Ottone, V. Cauda, D. Fino, M. Piumetti, Preparation of a mesoporous biosensor for human lactate dehydrogenase for potential anticancer inhibitor screening, ACS Biomater. Sci. Eng. 9 (2023) 6045–6057, https://doi.org/10.1021/acsbiomaterials.3c00582.

[41] K.J. Nelson, D. Parsonage, Measurement of peroxiredoxin activity, Curr. Protoc. Toxicol. 49 (2011), https://doi.org/10.1002/0471140856.tx0710s49.

[42] I. Marko, K.A. Johnson, Enzyme kinetic analysis for the 21st century, Biochemistry 65 (2026) 637–648, https://doi.org/10.1021/acs.biochem.5c00765.

[43] F. Busto, D. De Arriaga, J. Soler, The kinetic mechanism of pyruvate reduction by lactate dehydrogenase from Phycomyces blakesleeanus, Int. J. BioChemiPhysics 16 (1984) 171–176, https://doi.org/10.1016/0020-711X(84)90068-5.

[44] H.-L. Peng, T. Egawa, E. Chang, H. Deng, R. Callender, Mechanism of thermal adaptation in the lactate dehydrogenases, J. Phys. Chem. B 119 (2015) 15256–15262, https://doi.org/10.1021/acs.jpcb.5b09909.

[45] S. Dempster, S. Harper, J.E. Moses, I. Dreveny, Structural characterization of the apo form and NADH binary complex of human lactate dehydrogenase, Acta Crystallogr. D Biol. Crystallogr. 70 (2014) 1484–1490, https://doi.org/10.1107/S1399004714005422.

[46] L. Qiu, M. Gulotta, R. Callender, Lactate dehydrogenase undergoes a substantial structural change to bind its substrate, Biophys. J. 93 (2007) 1677–1686, https://doi.org/10.1529/biophysj.107.109397.

[47] A. Illanes, Enzyme biocatalysis, 2008.

[48] R. Knizikevičius, Comparison of linear transformations for deriving kinetic constants during silicon etching in Cl2 environment, Vacuum 157 (2018) 391–394, https://doi.org/10.1016/j.vacuum.2018.08.056.

[49] S.K. Burley, H.M. Berman, C. Bhikadiya, C. Bi, L. Chen, L. Di Costanzo, C. Christie, J.M. Duarte, S. Dutta, Z. Feng, S. Ghosh, D.S. Goodsell, R.K. Green, V. Guranovic, D. Guzenko, B.P. Hudson, Y. Liang, R. Lowe, E. Peisach, I. Periskova, C. Randle, A. Rose, M. Sekharan, C. Shao, Y.-P. Tao, Y. Valasatava, M. Voigt, J. Westbrook, J. Young, C. Zardecki, M. Zhuravleva, G. Kurisu, H. Nakamura, Y. Kengaku, H. Cho, J. Sato, J.Y. Kim, Y. Ikegawa, A. Nakagawa, R. Yamashita, T. Kudou, G.-J. Bekker, H. Suzuki, T. Iwata, M. Yokochi, N. Kobayashi, T. Fujiwara, S. Velankar, G.J. Kleywegt, S. Anyango, D.R. Armstrong, J.M. Berrisford, M. J. Conroy, J.M. Dana, M. Deshpande, P. Gane, R. Gáborová, D. Gupta, A. Gutmanas, J. Koča, L. Mak, S. Mir, A. Mukhopadhyay, N. Nadzirin, S. Nair, A. Patwardhan, T. Paysan-Lafosse, L. Pravda, O. Salih, D. Sehnal, M. Varadi, R. Vařeková, J.L. Markley, J.C. Hoch, P.R. Romero, K. Baskaran, D. Maziuk, E. L. Ulrich, J.R. Wedell, H. Yao, M. Livny, Y.E. Ioannidis, Protein data Bank: the single global archive for 3D macromolecular structure data, Nucleic Acids Res. 47 (2019) D520–D528, https://doi.org/10.1093/nar/gky949.

[50] S. Kim, J. Chen, T. Cheng, A. Gindulyte, J. He, S. He, Q. Li, B.A. Shoemaker, P. A. Thiessen, B. Yu, L. Zaslavsky, J. Zhang, E.E. Bolton, PubChem 2023 update, Nucleic Acids Res. 51 (2023) D1373–D1380, https://doi.org/10.1093/nar/gkac956.

[51] A. Erdem, S. Kaye, F. Caligiore, M. Johanns, F. Leguay, J.J. Schuringa, K. Ito, G. Bommer, N. van Gastel, Lactate dehydrogenase A-coupled NAD+ regeneration is critical for acute myeloid leukemia cell survival, Cancer Metab. 13 (2025) 22, https://doi.org/10.1186/s40170-025-00392-4.

[52] E. Kocianova, V. Piatrikova, T. Golias, Revisiting the Warburg effect with focus on lactate, Cancers (Basel) 14 (2022) 6028, https://doi.org/10.3390/cancers14246028.

[53] T. Waluga, F. von Ziegner, M. Skiborowski, Analytical and numerical approaches to the analysis of progress curves: a methodological comparison, Process Biochem. 151 (2025) 1–13, https://doi.org/10.1016/j.procbio.2025.01.029.

[54] R.M. Silverstein, F.X. Webster, D.J. Kiemle, D.L. Bryce, Spectrometric Identification of Organic Compounds, Wiley, 2017.

[55] J. De Ruyck, M. Famerée, J. Wouters, E.A. Perpète, J. Preat, D. Jacquemin, Towards the understanding of the absorption spectra of NAD(P)H/NAD(P)+ as a common indicator of dehydrogenase enzymatic activity, Chem. Phys. Lett. 450 (2007) 119–122, https://doi.org/10.1016/j.cplett.2007.10.092.

[56] R.A. Copeland, Evaluation of enzyme inhibitors in drug discovery, Wiley, 2013, https://doi.org/10.1002/9781118540398.

[57] R.A. Copeland, Mechanistic considerations in high-throughput screening, Anal. Biochem. 320 (2003) 1–12, https://doi.org/10.1016/S0003-2697(03)00346-4.

[58] S. Buzrul, The Michaelis–Menten equation and its linear transformations revisited, Chem. Biodivers. 23 (2026), https://doi.org/10.1002/cbdv.202503211.

[59] G.F. Healey, Fitting models to biological data using linear and nonlinear regression Motulsky H, Christopoulos A (2004)ISBN 0195171802; 352 pages; £18.50 Oxford University Press, Pharm. Stat. 4 (2005) 147–148, https://doi.org/10.1002/pst.167.

[60] N.R. Draper, H. Smith, Applied regression analysis, Wiley, 1998, https://doi.org/10.1002/9781118625590.

[61] Robert. Eisenthal, M.J.. Danson, Enzyme Assays : A Practical Approach, Oxford University Press, 2002.

[62] E. Khodadadian, S. Mirsian, S. Shashaani, M. Parvizi, A. Khodadadian, P. Knees, W. Hilber, C. Heitzinger, A Bayesian inversion supervised learning framework for the enzyme activity in graphene field-effect transistors, Mach. Learn. Appl. 21 (2025) 100718, https://doi.org/10.1016/j.mlwa.2025.100718.

[63] Y.-S. Cho, H.-S. Lim, Comparison of various estimation methods for the parameters of Michaelis-Menten equation based on *in vitro* elimination kinetic simulation data, Transl. Clin. Pharmacol. 26 (2018) 39, https://doi.org/10.12793/tcp.2018.26.1.39.

[64] M. Marolt, S. Lüdeke, Studying NAD(P)H cofactor-binding to alcohol dehydrogenases through global analysis of circular dichroism spectra, Phys. Chem. Chem. Phys. 21 (2019) 1671–1681, https://doi.org/10.1039/C8CP04869J.

[65] R. Hegazy, J.R. Cristobal, J.P. Richard, Glycerol 3-phosphate dehydrogenase catalyzed hydride transfer: enzyme activation by cofactor pieces, Biochemistry 63 (2024) 2878–2891, https://doi.org/10.1021/acs.biochem.4c00324.

[66] S. García, C. Cocuzza, L. Wilson, M. Piumetti, C. Ottone, Electroassisted cofactor regeneration with co-immobilized FDH-GlyDH on mesoporous silica for enhanced CO2 conversion, Microporous Mesoporous Mater. 396 (2025) 113706, https://doi.org/10.1016/j.micromeso.2025.113706.

[67] C.M. Eszes, R.B. Sessions, A.R. Clarke, K.M. Moreton, J.J. Holbrook, Removal of substrate inhibition in a lactate dehydrogenase from human muscle by a single residue change, FEBS Lett. 399 (1996) 193–197, https://doi.org/10.1016/S0014-5793(96)01317-8.

[68] A.P. Pasti, V. Rossi, G. Di Stefano, M. Brigotti, A. Hochkoeppler, Human lactate dehydrogenase a undergoes allosteric transitions under pH conditions inducing the dissociation of the tetrameric enzyme, Biosci. Rep. 42 (2022), https://doi.org/10.1042/BSR20212654.

[69] Y. Rao, S.T. Gammon, M.N. Sutton, N.M. Zacharias, P. Bhattacharya, D. Piwnica-Worms, Excess exogenous pyruvate inhibits lactate dehydrogenase activity in live cells in an MCT1-dependent manner, J. Biol. Chem. 297 (2021) 100775, https://doi.org/10.1016/j.jbc.2021.100775.

[70] K. Świderek, P. Paneth, Differences and similarities in binding of pyruvate and l-lactate in the active site of M4 and H4 isoforms of human lactate dehydrogenase, Arch. Biochem. Biophys. 505 (2011) 33–41, https://doi.org/10.1016/j.abb.2010.10.010.

[71] S.H. Chiou, H.J. Lee, G.G. Chang, Kinetic analysis of duck ε -crystallin, a lens structural protein with lactate dehydrogenase activity, Biochem. J. 267 (1990) 51–58, https://doi.org/10.1042/bj2670051.

[72] W.W. Cleland, The kinetics of enzyme-catalyzed reactions with two or more substrates or products, Biochimica et Biophysica acta (BBA) - Specialized Section on Enzymological Subjects 67 (1963) 104–137, https://doi.org/10.1016/0926-6569(63)90211-6.

[73] I.H. Segel, Enzyme kinetics: behavior and analysis of rapid equilibrium and steady state enzyme systems, Wiley, 1993.

[74] J.R.E.T. Pineda, R. Callender, S.D. Schwartz, Ligand binding and protein dynamics in lactate dehydrogenase, Biophys. J. 93 (2007) 1474–1483, https://doi.org/10.1529/biophysj.107.106146.

[75] A. Vetrano, M. Capone, M. Farina, F. Gabriele, N. Spreti, I. Daidone, Unveiling cofactor inhibition mechanisms in horse liver alcohol dehydrogenase: an allosteric driven regulation, Bioorg. Chem. 153 (2024) 107932, https://doi.org/10.1016/j.bioorg.2024.107932.

[76] J.R. Cristobal, R.W. Nagorski, J.P. Richard, Utilization of cofactor binding energy for enzyme catalysis: formate dehydrogenase-catalyzed reactions of the whole NAD cofactor and cofactor pieces, Biochemistry 62 (2023) 2314–2324, https://doi.org/10.1021/acs.biochem.3c00290.

[77] Y. Nishiguchi, N. Ito, M. Okada, Structure and function of lactate dehydrogenase from hagfish, Mar. Drugs 8 (2010) 594–607, https://doi.org/10.3390/md8030594.
[78] H. Cai, S. Shulami, Z. Štefanić, T. Hrenar, A. Maršavelski, A. Fishman, Allosteric regulation of L-lactate dehydrogenase: beyond effector-mediated tetramerization, Protein Sci. 34 (2025), https://doi.org/10.1002/pro.70206.
[79] S. Hui, J.M. Ghergurovich, R.J. Morscher, C. Jang, X. Teng, W. Lu, L.A. Esparza, T. Reya, Le Zhan, J. Yanxiang Guo, E. White, J.D. Rabinowitz, Glucose feeds the TCA cycle via circulating lactate, Nature 551 (2017) 115–118, https://doi.org/10.1038/nature24057.
[80] A. Pesaresi, Mixed and non-competitive enzyme inhibition: underlying mechanisms and mechanistic irrelevance of the formal two-site model, J. Enzyme Inhib. Med. Chem. 38 (2023), https://doi.org/10.1080/14756366.2023.2245168.
[81] I.H. Segel, Protein function enzyme kinetics, in: Encyclopedia of biological chemistry III, Elsevier, 2013, pp. 7–13, https://doi.org/10.1016/B978-0-12-819460-7.00560-0.
[82] S. Sevmezler, S. Çol, M. Emirik, D. Ceylan, A. Baran, Versatile synthesis of rac - and meso -hydroxymethyl cyclohexenoids containing phenyl groups: α−/β-glucosidase activities, inhibition kinetics and molecular docking studies, Eur. J. Org. Chem. 2022 (2022), https://doi.org/10.1002/ejoc.202200165.
[83] A. Lynch, P. Pearson, S.N. Savinov, A.Y. Li, S.M. Rich, Lactate dehydrogenase inhibitors suppress borrelia burgdorferi growth in vitro, Pathogens 12 (2023), https://doi.org/10.3390/pathogens12070962.
[84] L. Li, Q. Lei, Y. Zhen, L. Cao, Y. Dong, X. Liu, M. Wang, Lactate dehydrogenase inhibition protects against hepatic fibrosis by regulating metabolic reprogramming of hepatic stellate cells, J. Agric. Food Chem. (2024), https://doi.org/10.1021/acs.jafc.4c08211.
[85] L. Di Magno, A. Coluccia, M. Bufano, S. Ripa, G. La Regina, M. Nalli, F. Di Pastena, G. Canettieri, R. Silvestri, L. Frati, Discovery of novel human lactate dehydrogenase inhibitors: structure-based virtual screening studies and biological assessment, Eur. J. Med. Chem. 240 (2022), https://doi.org/10.1016/j.ejmech.2022.114605.
[86] A. Friberg, H. Rehwinkel, D. Nguyen, V. Pütter, M. Quanz, J. Weiske, U. Eberspächer, I. Heisler, G. Langer, Structural evidence for isoform-selective allosteric inhibition of lactate dehydrogenase a, ACS Omega 5 (2020) 13034–13041, https://doi.org/10.1021/acsomega.0c00715.
[87] S. Rupiani, L. Guidotti, M. Manerba, L. Di Ianni, E. Giacomini, F. Falchi, G. Di Stefano, M. Roberti, M. Recanatini, Synthesis of natural urolithin M6, a galloflavin mimetic, as a potential inhibitor of lactate dehydrogenase A, Org. Biomol. Chem. 14 (2016) 10981–10987, https://doi.org/10.1039/c6ob01977c.
[88] M. Manerba, L. Di Ianni, M. Govoni, M. Roberti, M. Recanatini, G. Di Stefano, LDH inhibition impacts on heat shock response and induces senescence of hepatocellular carcinoma cells, Eur. J. Pharm. Sci. 105 (2017) 91–98, https://doi.org/10.1016/j.ejps.2017.05.015.
[89] M. Manerba, M. Vettraino, L. Fiume, G. Di Stefano, A. Sartini, E. Giacomini, R. Buonfiglio, M. Roberti, M. Recanatini, Galloflavin (CAS 568-80-9): a novel inhibitor of lactate dehydrogenase, ChemMedChem 7 (2012) 311–317, https://doi.org/10.1002/cmdc.201100471.
[90] C. Granchi, E.C. Calvaresi, T. Tuccinardi, I. Paterni, M. Macchia, A. Martinelli, P. J. Hergenrother, F. Minutolo, Assessing the differential action on cancer cells of LDH-A inhibitors based on the N-hydroxyindole-2-carboxylate (NHI) and malonic (mal) scaffolds, Org. Biomol. Chem. 11 (2013) 6588, https://doi.org/10.1039/c3ob40870a.
[91] H.J. Jang, Y.M. Song, J.S. Jeon, H. Yun, S.K. Kim, J.K. Kim, Optimizing enzyme inhibition analysis: precise estimation with a single inhibitor concentration, Nat. Commun. 16 (2025) 5217, https://doi.org/10.1038/s41467-025-60468-z.
[92] S.G. Waley, The kinetics of slow-binding and slow, tight-binding inhibition: the effects of substrate depletion, Biochem. J. 294 (1993) 195–200, https://doi.org/10.1042/bj2940195.
[93] K.L. Olgiati, W.A. Toscano, Kinetics of gossypol inhibition of bovine lactate dehydrogenase X, Biochem. Biophys. Res. Commun. 115 (1983) 180–185, https://doi.org/10.1016/0006-291X(83)90986-5.
[94] G.S. Gupta, S. Kapur, R.G. Kinsky, Inhibition kinetics of lactate dehydrogenase isoenzymes by gossypol acetic acid, Biochem. Int. 17 (1988) 25–34.
[95] M.S. Ha, C.W. Han, M.S. Jeong, S. Cheon, K.T. Ha, H.Y. Kim, S.B. Jang, Structural basis of lactate dehydrogenase A-gossypol complex, Biochem. Biophys. Res. Commun. 733 (2024), https://doi.org/10.1016/j.bbrc.2024.150721.
[96] J.H. Han, E.J. Lee, W. Park, K.T. Ha, H.S. Chung, Natural compounds as lactate dehydrogenase inhibitors: potential therapeutics for lactate dehydrogenase inhibitors-related diseases, Front. Pharmacol. 14 (2023), https://doi.org/10.3389/fphar.2023.1275000.
[97] Y. Liu, L. Wang, L. Zhao, Y. Zhang, Structure, properties of gossypol and its derivatives—from physiological activities to drug discovery and drug design, Nat. Prod. Rep. 39 (2022) 1282–1304, https://doi.org/10.1039/D1NP00080B.
[98] M. Ikeda, Inhibition kinetics of NAD-linked enzymes by gossypol acetic acid, Andrologia 22 (2009) 409–416, https://doi.org/10.1111/j.1439-0272.1990.tb02019.x.
[99] A. Le, C.R. Cooper, A.M. Gouw, R. Dinavahi, A. Maitra, L.M. Deck, R.E. Royer, D. L. Vander Jagt, G.L. Semenza, C.V. Dang, Inhibition of lactate dehydrogenase A induces oxidative stress and inhibits tumor progression, Proc. Natl. Acad. Sci. USA 107 (2010) 2037–2042, https://doi.org/10.1073/pnas.0914433107.
[100] L. Fiume, M. Vettraino, M. Manerba, G. Di Stefano, Inhibition of lactic dehydrogenase as a way to increase the anti-proliferative effect of multi-targeted kinase inhibitors, Pharmacol. Res. 63 (2011) 328–334, https://doi.org/10.1016/j.phrs.2010.12.005.
[101] G.S. Murthy, D.B. Johnston, K.D. Rausch, M.E. Tumbleson, V. Singh, Starch hydrolysis modeling: application to fuel ethanol production, Bioprocess Biosyst. Eng. 34 (2011) 879–890, https://doi.org/10.1007/s00449-011-0539-6.
[102] L.L. Pham, S.M. Watford, P. Pradeep, M.T. Martin, R.S. Thomas, R.S. Judson, R. W. Setzer, K. Paul Friedman, Variability in in vivo studies: defining the upper limit of performance for predictions of systemic effect levels, computational Toxicology 15 (2020) 100126, https://doi.org/10.1016/j.comtox.2020.100126.
[103] J.L. Rendón, J.P. Pardo, Time-dependent kinetic complexities in enzyme assays: a review, Biomolecules 15 (2025) 641, https://doi.org/10.3390/biom15050641.
[104] R. Stambaugh, D. Post, Substrate and product inhibition of rabbit muscle lactic dehydrogenase heart (H4) and muscle (M4) isozymes, J. Biol. Chem. 241 (1966) 1462–1467, https://doi.org/10.1016/S0021-9258(18)96733-5.
[105] C.-S. Wang, Inhibition of human erythrocyte lactate dehydrogenase by high concentrations of pyruvate. Evidence for the competitive substrate inhibition, Eur. J. Biochem. 78 (1977) 569–574, https://doi.org/10.1111/j.1432-1033.1977.tb11770.x.